by J. L. Jordan-Sweet

Synchrotron X-ray scattering techniques for microelectronicsrelated materials studies

X-ray diffraction techniques using synchrotron radiation play a vital role in the understanding of structural behavior for a wide range of materials important in microelectronics. The extremely high flux of X-rays produced by synchrotron storage rings makes it possible to probe layers and interfaces in complicated stacked structures, characterize low-atomicweight materials such as polymers, and study in situ phase transformations, to name only a few applications. In this paper, following an introduction to synchrotron radiation, we describe the capabilities of the IBM/MIT X-ray beamlines at the National Synchrotron Light Source (NSLS), Brookhaven National Laboratory (BNL). A range of techniques are introduced, and examples of their applicability to the study of microelectronics-related materials phenomena are described.

Introduction

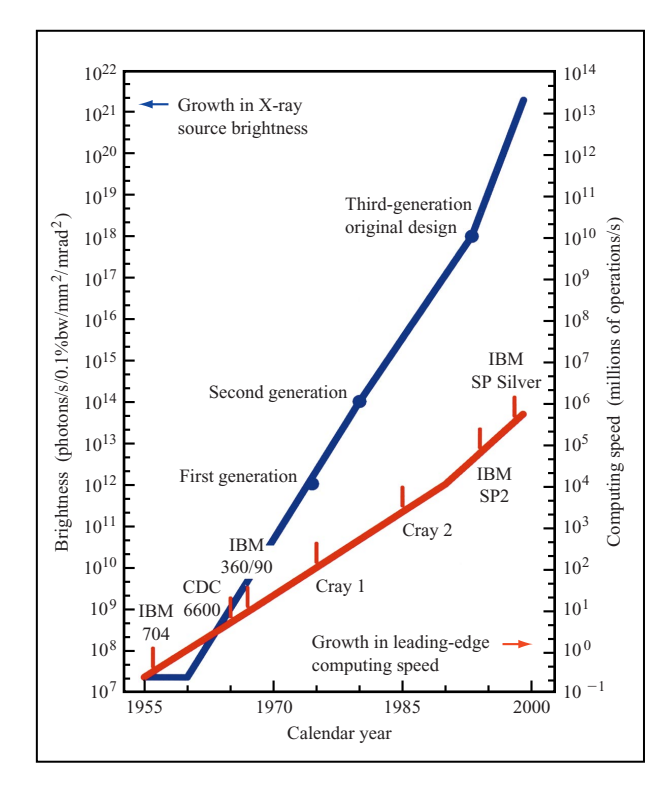
A short history

Synchrotron radiation, arising from the loss of energy by relativistic electrons through radiation, was first observed

in 1947 [1, 2]. It was considered to be an unfortunate and annoying side effect of accelerators that were developed for high-energy physics experiments. As charged particles pass between the poles of magnets that are designed to "bend" them into a circular orbit around an evacuated synchrotron ring, the magnetic field causes them to accelerate (change direction) and emit electromagnetic radiation in a direction tangential to their path. Synchrotron radiation energy is usually distributed in a black-body curve having a critical energy that is determined by the energy of the orbiting electrons or positrons. By the late 1950s, synchrotron radiation itself was being used for experiments, but until the 1970s work was carried out in a "parasitic" mode with respect to high-energy physics experiments. These first-generation synchrotron rings, such as SPEAR at the Stanford Synchrotron Radiation Laboratory (SSRL), CESR at the Cornell High Energy Synchrotron Source (CHESS), and DORIS at the Hamburger Synchrotronstrahlungslabor (HASYLAB), were not optimized for the production of synchrotron radiation, yet provided experimenters with photon densities (brightnesses) around five orders of magnitude higher than conventional laboratory X-ray

©Copyright 2000 by International Business Machines Corporation. Copying in printed form for private use is permitted without payment of royalty provided that (1) each reproduction is done without alteration and (2) the Journal reference and IBM copyright notice are included on the first page. The title and abstract, but no other portions, of this paper may be copied or distributed royalty free without further permission by computer-based and other information-service systems. Permission to republish any other portion of this paper must be obtained from the Editor.

0018-8646/00/\$5.00 © 2000 IBM



Increase since 1955 in X-ray source brightness (blue) and growth in leading-edge computing speed (red). Adapted from [5], with permission, and updated courtesy of A. E. Brenner, Institute for Defense Analysis.

sources [1]. They also produced a continuous spectrum of X-ray energies.

In the late 1970s to early 1980s, dedicated secondgeneration storage rings were developed using a special "Chasman-Green" lattice of dipole, quadrupole, and sextupole magnets that produced a brightness increase of two orders of magnitude. The National Synchrotron Light Source (NSLS) at Brookhaven National Laboratory (BNL) on Long Island, New York, and Photon Factory (KEK) in Japan are examples of second-generation facilities.

The next improvement came with the demonstration of "insertion devices" at SSRL in 1979–1980 [3]. Insertion devices consist of linear arrays of dipole magnets alternating in orientation and having a variable "gap" between the poles through which the electrons or positrons travel. When inserted into a straight section of the storage ring (between the bending magnets), they cause the electron or positron beam to follow a sinusoidal path and produce approximately n times more photon flux, where n is the number of dipoles. "Wigglers" have a large amplitude for the sinusoidal electron path and produce a relatively wide fan of incoherent light, while low-amplitude

"undulators" produce extremely well-collimated coherent beams of light. Second-generation synchrotrons have been upgraded with insertion devices where possible, and are testing grounds for new designs. Currently, second-generation rings produce a maximum brightness of ~10¹⁴ photons/s/0.1%bw/mm²/mrad². (Brightness is a combination of flux, source size, and beam divergence. It is given in units of number of photons per second in a certain energy bandwidth, divided by source area and by the solid angle of the radiation cone.)

Recently, third-generation storage rings have been designed specifically to take advantage of insertion devices, primarily undulators. Rings such as the European Synchrotron Radiation Facility (ESRF) in Grenoble, the Advanced Photon Source (APS) at Argonne National Laboratory, and Super Photon ring-8 GeV (SPring-8) in Japan have relatively long straight sections (to incorporate the largest number of dipoles) and "low-emittance" lattices [1]. These X-ray rings have been commissioned in just the last few years and are the giants of the synchrotron radiation community in terms of size (~1100–1400-m circumference), brightness (~10¹⁸–10²⁰ photons/s/0.1%bw/mm²/mrad²), and potential number of users (several thousand per year).

The future looks even brighter. Workshops are being held on the design of fourth-generation light sources [4]. Although these are unlikely to be rings, since the size and cost would be prohibitive, it is possible to build linear-accelerator-driven "free-electron lasers" that could reach a brightness of 10²³. **Figure 1** is a plot showing the growth in brightness of X-ray sources since 1955¹ [5]. For comparison, the phenomenal growth in top-end computing speed follows a much shallower slope! The synchrotron research community has grown to the point where it has two dedicated journals [6] with contributions from more than 29 facilities located around the world. All of this immense activity serves important scientific and technological needs of industry, academia, and government laboratories.

• Properties of synchrotron radiation

We have already seen how synchrotron radiation is orders of magnitude brighter than X-rays produced by a laboratory source. This brightness has opened up new fields of research and allowed for the investigation of previously unmeasurable samples. More photons produce higher signals, which make it possible to measure a sample more rapidly or examine smaller, thinner, and lower-density samples. Three basic approaches can be used: diffraction, which yields crystallographic structural information; spectroscopy, which can be used to probe electronic structure and bonding; and imaging or microscopy, which can be used to measure the spatial

¹ A. E. Brenner, private communication.

variation of a chosen characteristic across a sample. Since the electrons or positrons circulating around the evacuated storage ring are grouped in "bunches," the emitted photons have a pulsed time structure, and thus pumpprobe experiments can be performed on a time scale of nanoseconds.

Because the energy distribution of photons in synchrotron radiation follows a black-body curve which has a characteristic "critical" energy, storage rings are designed to take advantage of specific segments of the electromagnetic spectrum. "Soft" X-ray rings, such as the Advanced Light Source (ALS) at Berkeley and the Vacuum Ultraviolet (VUV) ring at the NSLS, are used primarily for photoelectron spectroscopy studies, photochemistry, imaging at absorption edges of light elements, and magnetic and standard circular dichroism. Applications for the microelectronics industry include projection lithography [7] and shadow-mask (proximity) lithography [8] for producing submicron features on chips. Several spectral curves showing brightness as a function of energy for dipole (bending magnet) and insertion device sources at the NSLS are shown in Figure 2. The soft-X-ray regime is below ~ 1500 eV (wavelengths greater than ~ 8 Å). Soft-X-ray rings typically run at relativistic electron energies of 0.8 to 2.0 giga-electron volts (GeV).

"Hard" X-rays are produced by electrons or positrons accelerated to higher energies, from 2.6 to 8 GeV. At these facilities, diffraction and extended X-ray adsorption fine structure (EXAFS) spectroscopy are the primary techniques used. Topography, tomography, and medical imaging are other important techniques that make use of hard X-rays. Curves of photon brightness vs. energy for the NSLS X-ray Ring bending magnets and insertion devices are also shown in Figure 2. The techniques and experiments described in this paper demonstrate various ways of using X-ray diffraction at a bending magnet beamline at the NSLS X-ray Ring to study materials of importance in microelectronics. An application for microelectronics using hard X-rays that is not discussed here is total external reflection X-ray fluorescence (TXRF), which is used for detection of trace impurities on the surfaces of semiconductor wafers [9].

• The National Synchrotron Light Source and the IBM Research Division

One of the unique features of the NSLS is the presence of two storage rings that make available an extremely wide range of photon energies.² The VUV Ring is 51 meters in circumference, operates at 0.8 GeV, and has maximum stored current of 1000 milliamperes (mA). It is optimized to deliver radiation at energies between 10 eV and 1 keV.

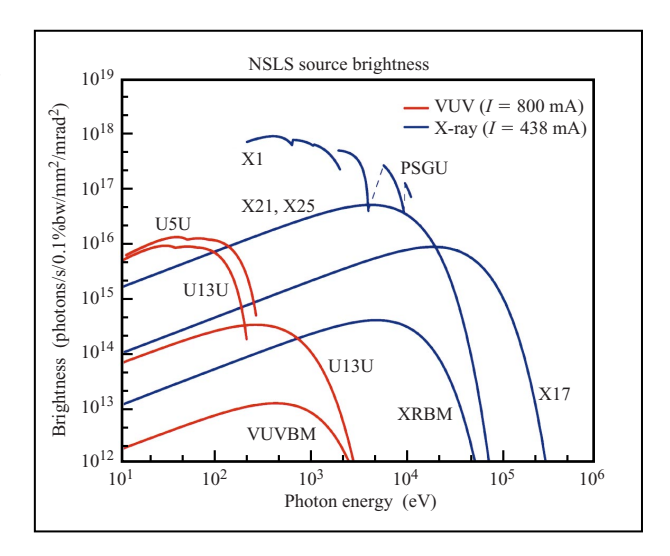


Figure 2

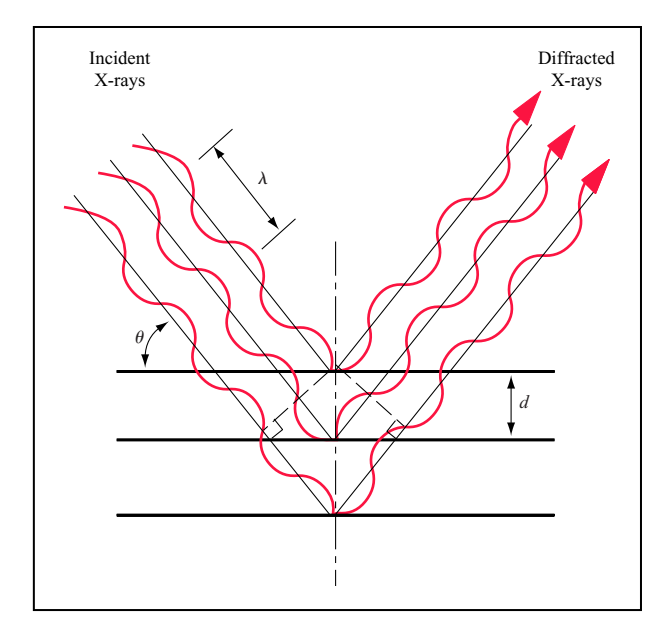
Spectral brightness curves for VUV bending magnet source (VUVBM), X-ray bending magnet source (XRBM), and insertion devices at the NSLS for 800 mA at 750 MeV (VUV Ring) and 438 mA at 2.58 GeV (X-ray Ring). X17, X21, and X25 are wiggler insertion devices. X1 is an undulator, and PSGU is the Prototype Small-Gap Undulator. U5U and U13U are undulators on the VUV ring. Port X20 uses an XRBM as its source. Courtesy of S. Hulbert, Brookhaven National Laboratory.

There are 17 beam ports—two at essentially every vertex in the ring where dipole magnets emit fans of synchrotron radiation, and two insertion devices. Each port can be subdivided to deliver smaller fans of radiation down evacuated beampipes to individual experiments. These subdivisions are called beamlines and usually are designed for a particular type of experimental technique. Along with standard photoelectron spectroscopy, lithography, spin-polarized photoemission, and circular dichroism beamlines, a specialty of the VUV Ring is the production of infrared radiation, which is used at five of its 25 beamlines [10].

The X-ray Ring has a circumference of 170 meters, operates at 2.58 or 2.8 GeV, and has a maximum stored current of 250–400 mA. There are 60 beamlines on 30 ports, including five insertion devices. It is optimized to deliver photons in the energy range of ~1–20 keV; however, specialized beamlines also produce >100-keV X-rays and 200–400-MeV gamma rays. Techniques used at the X-ray Ring include many types of diffraction, inelastic scattering, EXAFS, topography, computed tomography, absorption contrast imaging, small-angle scattering, fluorescence, atomic spectroscopy, microscopy, and radiography.

The NSLS hosts more than 2200 experimenters each year from three basic categories: NSLS staff, general users

² Descriptions of the facility and beamlines can be found on the NSLS home page: http://www.nsls.bnl.gov/Intro/nslsdesc.htm.



Fiaure 3

Schematic showing constructive interference of X-ray plane waves under conditions of Bragg diffraction.

(visiting scientists not affiliated with BNL or any of the "owners" of beamlines), and beamline owners (scientists who work for industry, government laboratories, or universities who have put resources into beamlines). These last workers make up the participating research teams (PRTs) that have designed, built, and run beamlines at the NSLS, in exchange for photons provided by the U.S. Department of Energy. These PRTs also make at least 25% of their beam time available to, and provide support for, general users. The NSLS staff also builds and operates some of the beamlines.

The IBM Research Division has been involved with the National Synchrotron Light Source since its commissioning in 1982. Originally, the Physical Sciences Department at the Division's Thomas J. Watson Research Center at Yorktown Heights, New York, operated two photoelectron spectroscopy beamlines (commissioned by Franz Himpsel, Read McFeely, and John Morar) and a beamline for zoneplate optics development and reflectivity measurements (commissioned by Eberhardt Spiller) at Port U8. Scientists from the Silicon Technology Department also developed soft-X-ray lithography at Port U6 on the VUV ring [8, 11]. As X-ray lithography at U6 was demonstrated in 1988 to produce fully integrated circuits having features down to 0.5 µm, an additional port at U2 was dedicated to industrializing that effort and was operated by engineers from the IBM Microelectronics facility in Hopewell Junction, New York. When the Advanced Lithography

Facility (ALF) was built in Hopewell Junction, the IBM soft-X-ray lithography effort was moved there.

As the X-ray Ring was being commissioned in the mid-1980s, Paul Horn (currently Director of the IBM Research Division) and Robert Birgeneau (Professor of Physics at MIT) combined forces (joined later by G. Brian Stephenson) and developed two beamlines designed for diffraction at Port X20. In 1989 a third beamline was developed at the same port. Originally the X-ray beamlines at that port were used for nonapplied studies, such as two-dimensional phase transitions of noble gases on graphite substrates, and the detailed structure of quasi-crystals. In the early 1990s, as the Research Division focused on studying processes and materials having a greater impact on technology, the efforts at Port X20 followed suit.

Described next are several different X-ray scattering techniques used in IBM studies at the beamlines of Port X20. Examples are given of the application of each technique to address an important materials issue. Our intention is to provide the reader with an appreciation of the wide range of materials, structures, and characteristics that can be measured using synchrotron X-rays, and to demonstrate their impact on microelectronics technology. Four categories of diffraction techniques and their applications are presented: 1) triple-axis diffraction, for measuring strain relaxation in SiGe structures; 2) grazingincidence diffraction, for determining near-surface ordering in the polymers used for flat-panel displays; 3) time-resolved, in situ diffraction, to study phase transformations in metal silicide contacts; and 4) microdiffraction, to measure strain fields produced in silicon by evaporated Ni metal features. First, the subject of diffraction is introduced and the beamline instrumentation described.

Diffraction and associated instrumentation

X-ray diffraction is used to measure the atomic plane spacings in crystalline materials [12]. According to Bragg's law, illustrated in **Figure 3**, a plane wave of X-rays having a wavelength λ scatters from atoms in a set of lattice planes of spacing d with constructive interference when

$$n\lambda = 2d \sin \theta$$
;

 θ is the diffraction "Bragg" angle, and n is the order of the reflection. Thus, with monochromatic radiation, one can determine the d-spacings of sets of planes in crystalline materials by knowing the wavelength and measuring the angles at which the X-rays diffract. Diffraction peaks are measured by orienting the sample angles $(\omega, \chi, \text{ and } \phi)$ and detector angle (2θ) with respect to the incident (fixed) beam so that an intensity maximum is intercepted by the detector. From the d-spacing values, unit cell parameters can be calculated using equations that

460

relate the symmetry of the unit cell to *d*-spacings. Other information, such as film thickness, grain size, mosaicity, and lattice distortions, is contained in diffraction peak shapes, widths, and intensities, and can be obtained by various types of diffractometer scans. **Figure 4** shows the four-circle diffractometer geometry for orienting a sample and detector. Most of the studies performed at Port X20 involve measurements of 1) lattice spacing changes due to applied stress or epitaxial strain; 2) changes in peak positions due to phase transformations in crystalline material; or 3) orientation and texture in polycrystalline films. Reflectivity is a nondiffraction X-ray technique that also is used at Port X20, to measure interfacial and surface roughnesses and layer thicknesses for single and stacked thin films.

Three X-ray diffraction beamlines are available at Port X20, designated as "A," "B," and "C." A simple schematic and specifications are shown in **Figure 5**. The beamline hardware consists of evacuated stainless steel pipe which is joined to the X-ray ring but separated from its vacuum by a thin beryllium window. At intervals along this pipe are placed a variety of optical components, slits, viewing screens, and chambers for measuring photon flux. The specific design of optical components varies between beamlines so that each has some properties that are unique to it.

The optical configurations of beamlines A and C are similar. At a distance of half the beamline length, each has a 600-mm-long cylindrically shaped mirror that is vertically bent to approximate an ellipsoidal reflecting surface. The mirrors are single-crystal silicon, cut from boules, ground and polished, and coated with platinum to provide total external reflection of X-rays up to ~12 keV at an incidence angle of $\sim 0.4^{\circ}$. At a 1:1 focusing position, they intercept a 4-mrad horizontal fan of X-rays and focus the beam to a spot size of 0.5 to 1.0 mm vertical and 0.8 mm horizontal full width at half maximum (FWHM) at the sample positions, which are 21.6 and 25.6 m from the X-ray (dipole magnet) source. The two beamlines also have double-crystal monochromators downstream of the mirrors. At beamline A, there are two Ge(111) flat crystals arranged in a nondispersive configuration. Beamline C can be configured for either two Si(111) crystals or two wide-bandpass synthetic multilayers. Two crystals are used because the distance between them can be adjusted so that the position of the exiting monochromatic beam is invariant with changes in X-ray energy. The Ge(111) and Si(111) crystals have an energy bandpass, $\Delta E/E$, of ~0.01%. With these monochromator crystals, typical beam intensities are $\sim 5 \times 10^{11}$ photons/s at 8 keV. Increased intensity can be achieved at beamline C by replacing the monochromator crystals with synthetic multilayers, which consist of alternating layers of silicon and tungsten having a bilayer spacing of ~22 Å. Their

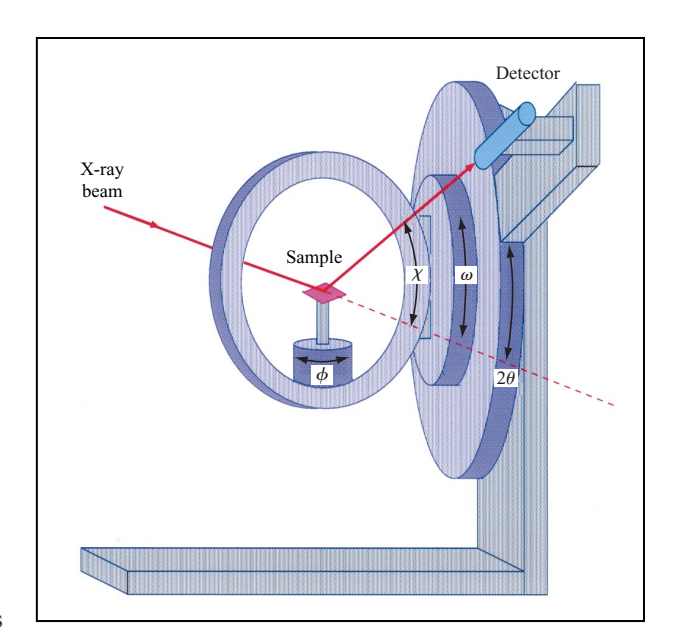


Figure 4

Illustration of the four-circle diffractometer geometry and relevant angles.

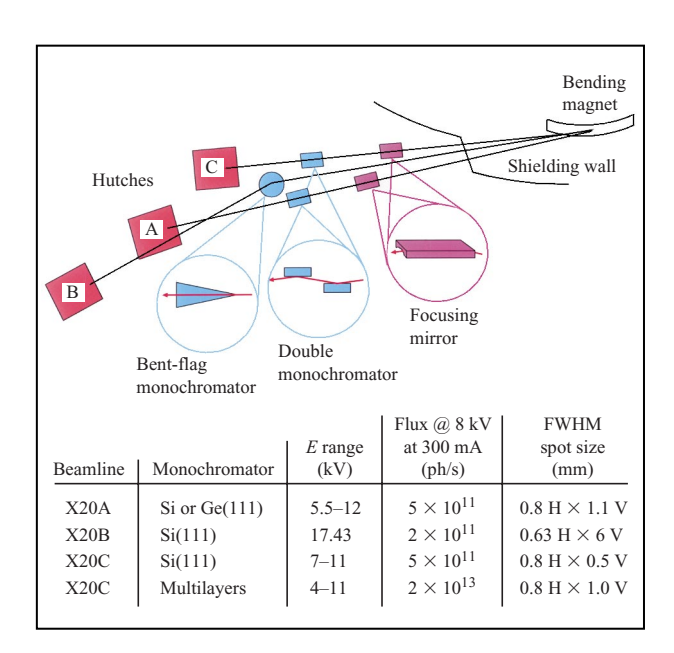


Figure 5

Schematic of optical configurations of the A, B, and C beamlines of Port $\rm X20$, and relevant specifications.

energy bandpass is \sim 1%, providing two orders of magnitude more flux. Multilayers are used when high

intensity is needed, although at a cost in resolution. Two examples are given of cases in which these are used: in time-resolved studies [13] and for grazing-incidence measurements of thin, poorly diffracting films [14]. Two other examples, using triple-axis diffraction and microdiffraction, require high-energy resolution; therefore, Si(111) or Ge(111) monochromator crystals must be used.

Beamline B is a fixed-energy beamline. A 2-mrad fan of radiation is diffracted and focused horizontally by a bent Si(111) pennant-shaped crystal. The fixed diffraction angle of 13° selects an X-ray energy of 17.4 keV. The spot size at the sample is \sim 5.5 mm vertical \times 0.7 mm horizontal FWHM, and the flux is \sim 2 \times 10¹¹ photons/s.

Experiments at each beamline are performed using instrumentation housed inside an interlocked steel hutch to protect the experimenter from incident and scattered radiation. All diffractometer maneuvering and beamline component adjustments are done by means of computercontrolled stepping motors. Each beamline has about thirty of these motors, and some experiments, such as microdiffraction, require even more. Alignment, diffractometer movements, and data collection are performed by use of a UNIX-** and C-based program called spec.³ The motor drivers and counting electronics are controlled via a GPIB interface by RS/6000* computers running AIX.* The beamlines were deliberately designed to be very flexible. Hutch instrumentation and monochromator crystals can be changed, and many types of diffraction geometries can be used. Thus, although there can be significant setup and alignment time involved, special techniques can be used and difficult setups can be put into place and shared by a number of groups having common instrumentation needs. For example, timeresolved and microbeam setups can be retained in a hutch for several months at a time. Two standard six-circle Huber diffractometers are available at X20 to all users. The IBM group also uses an instrument dedicated to microdiffraction, and the MIT group uses a superconducting cryomagnet/diffraction instrument for the study of magnetic materials.

Triple-axis diffraction: strain relaxation in $Si_{1-x}Ge_x$ structures

A strained $Si_{1-x}Ge_x$ layer is used as the base region in high-speed SiGe heterojunction bipolar transistors currently manufactured by IBM [15]. Relaxed $Si_{1-x}Ge_x$ buffer layers are also being investigated as substrates for high-mobility field-effect transistors (FETs) that have strained-layer channels resulting in carrier mobilities five to ten times those of conventional Si FETs [16]. A suitable substrate for strained-layer FETs must have the

correct in-plane lattice spacing to provide the desired lattice-mismatch strain in the thin pseudomorphic Si, Ge, or $\mathrm{Si}_{1-x}\mathrm{Ge}_x$ carrier channel layers. It also must be thermally stable, have a flat surface, and have a low defect density. For cubic materials, the lattice mismatch strain in a pseudomorphic film is $\varepsilon=(a_\ell-a_s)/a_s$, where a_ℓ is the bulk lattice parameter of the layer material and a_s is the lattice parameter of the substrate. Relaxed (strain-free) $\mathrm{Si}_{0.7}\mathrm{Ge}_{0.3}$ has the desired lattice parameter to serve as a substrate for FETs having strained Si or $\mathrm{Si}_{0.3}\mathrm{Ge}_{0.7}$ quantum wells as active carrier channels, but is not commercially available in bulk wafer form in sizes suitable for circuit fabrication.

Good substrates have been achieved by careful control of the growth of a series of $Si_{1-r}Ge_r$ layers of increasing Ge concentration on Si(001) wafers using ultrahighvacuum chemical-vapor deposition [16]. For lattice mismatch strain <0.02, the strain is relieved by the introduction of 60° misfit dislocations. These defects have misfit segments running parallel to the growth interface that relieve the strain and terminate with threading arms running up to the surface. When a Si_{1-r}Ge_r layer exceeds a "critical thickness" [17], relaxation occurs through two different mechanisms. If a Si_{1-x}Ge_x layer is grown on Si(001) at higher temperatures and has a higher mismatch strain, it relaxes by roughening and subsequent formation of 60° misfit dislocations in regions of high strain [16, 18]. In this case, the misfit segments lie at the Si, Ge/Si interface, and there is a high density of threading arms (threading dislocations) terminating at the surface. If the layer is grown at a lower temperature and has a lower mismatch strain, the surface remains smooth, and the 60° misfit dislocations are formed primarily by a Frank-Read multiplication mechanism [16, 19]. This mechanism results in pile-ups of dislocations on the (111) glide planes extending several microns below the Si_{1-r}Ge_r/Si interface and also in a relatively defect-free surface [19]. Grading the alloy composition continuously or stepwise from pure Si up to Si_{0.7}Ge_{0.3} results in a high-quality relaxed buffer layer having defect densities in the range of 5×10^5 5×10^7 defects/cm², depending on the grading rate [16]. Triple-axis diffraction has verified that strain relaxation occurs continuously during growth of the step-graded buffer layer and thus that dislocation nucleation always occurs at low mismatch strain in these structures, as is necessary for Frank-Read multiplication [20].

When a crystal has a significant mosaic structure, for example due to the distortion or bending of the lattice planes by the strain field of the dislocations, many diffracted rays may enter through the detector slit during an ω or ω -2 θ scan and broaden the diffraction peaks. For a sample consisting of several layers that have only slightly different unit cell dimensions, the mosaic broadening makes the individual diffraction peaks indistinguishable.

³ Certified Scientific Software, P.O. Box 390640, Cambridge, MA; http://www.certif.com.

In such a case, the addition of a third diffraction "axis," in the form of an analyzing crystal that greatly reduces the angular and energy acceptance of the detector, can greatly enhance the resolution of these peaks [21]. (The first axis is the monochromator, and the second is the sample.) The highest resolution in terms of q, the scattering vector having a magnitude of $(4\pi\sin\theta)/\lambda$, is obtained in a nondispersive configuration where each diffraction "bounce" off an axis changes the vertical direction sign of the beam (i.e., the incident beam is reflected down, then up, then down). P. M. Mooney and collaborators have used a Ge(111) monochromator and Si(111) analyzer on beamline A to measure small d-spacing shifts due to strain relaxation in compositionally graded Si_{1-x}Ge_x structures [16, 20, 22, 23]. **Figure 6** shows the advantage of using triple-axis diffraction to resolve peaks from the various layers in a SiGe/Si structure step-graded up to Si_{0.66}Ge_{0.34}. The use of a synchrotron source improves both the signalto-noise and data collection times by orders of magnitude.

Figure 7(a) shows the Ge mole fraction growth profile observed for a series of step-graded structures grown on Si(001), each sample having an additional layer (i.e., sample 3 had layers 1, 2, and 3; sample 4 had layers 1, 2, 3, and 4; etc.) [20]. Figure 7(b) shows the (004) radial $(\omega-2\theta)$ scans for samples 3 through 7. Distinct peaks can be seen not only for the Si substrate, but also for the ~ 0.25 - μ m-thick step-graded layers. Increasing the Bragg angle, $\theta_{\rm B}$, corresponds to decreasing the lattice spacing in the growth (z or [001]) direction. In order to calculate the layer composition (Ge mole fraction) and strain, one must determine the lattice parameters both in the growth direction and parallel to it $(a_x \text{ and } a_y)$. This is achieved by measuring diffraction peaks from two sets of lattice planes that are not equivalent or parallel. A commercial simulation program⁴ was used to determine the alloy composition and strain for each layer from its (004) and (044) reflections. Reciprocal space maps of the (044) region were made by taking a mesh of radial scans (ω -2 θ scans) at intervals of $\Delta\omega$. Figure 8 shows the log-scale intensity maps (displayed in **q**-vector notation for clarity) obtained for samples 3, 4, and 5. The component q_z is normal to the sample surface (parallel to the growth direction), and q_{v} is parallel to the surface. The peak position for a fully relaxed layer would lie upon the 45° dashed line $(q_z = q_y)$. A fully strained layer peak would have the same q_{y} value as that of the layer directly below it. Figure 8(a) shows that layer 3 was fully strained; the mismatch strain was 0.0052. Figure 8(b) shows that both layer 3 and layer 4 were fully strained; however, the increased broadening of peaks 3 and 4 indicated that the layers had a significant amount of mosaicity, even though only a few misfit dislocations had formed. As the fifth

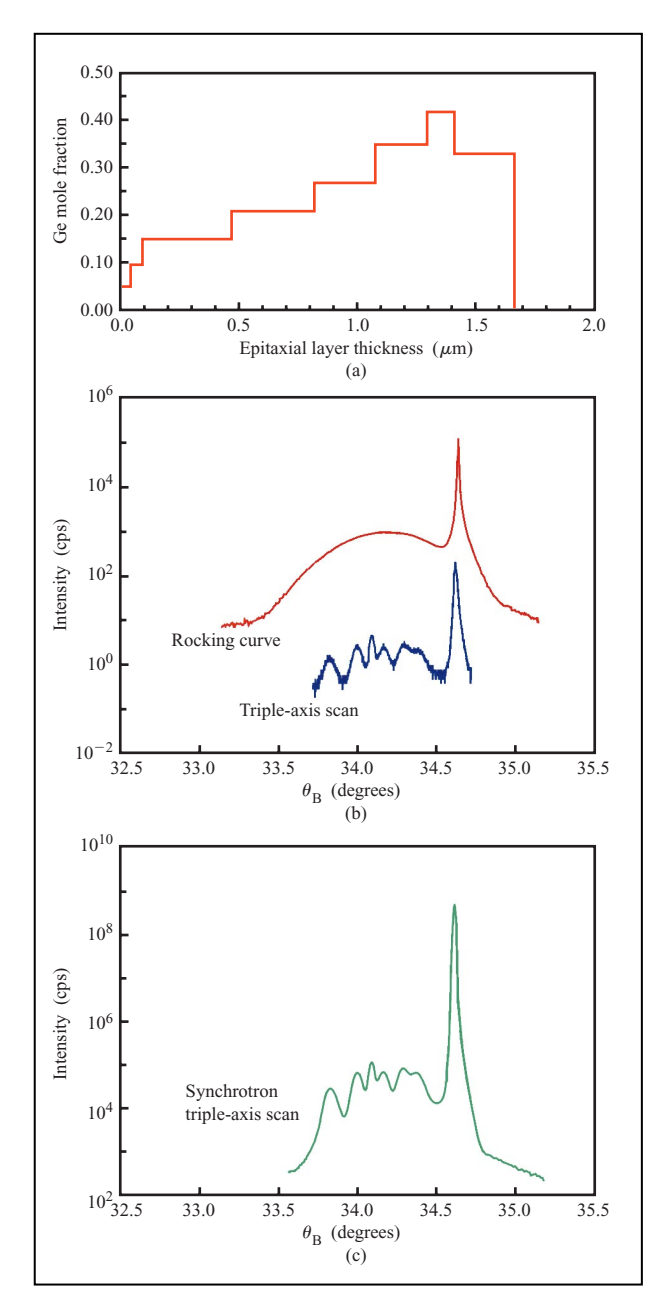
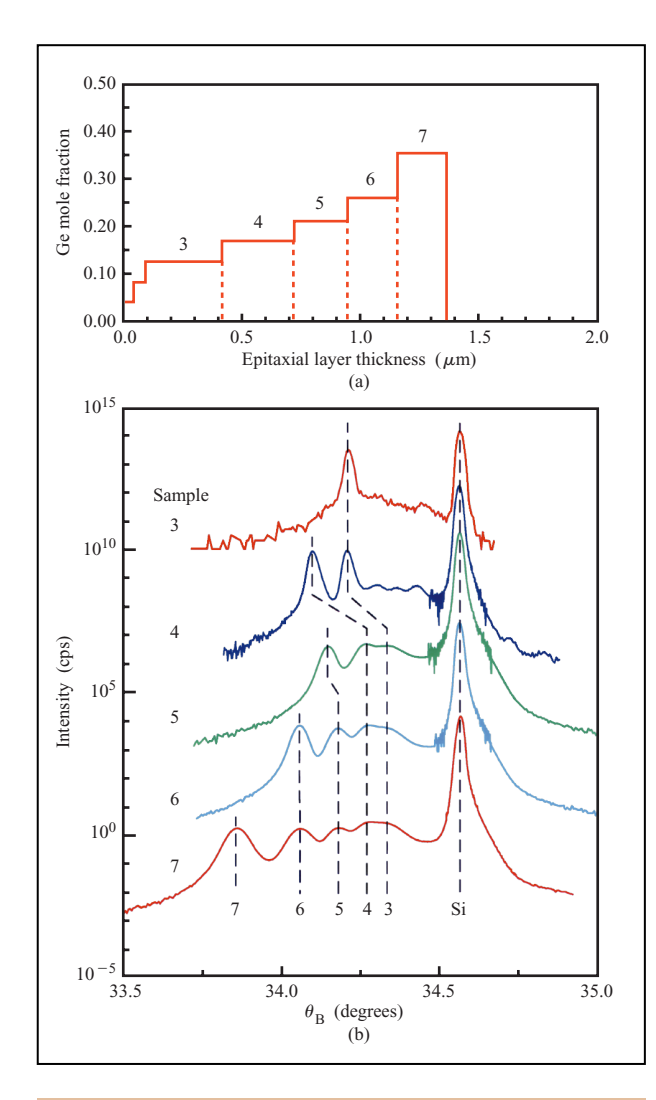


Figure 6

(a) Ge concentration profile for an eight-layer step-graded SiGe/Si structure graded up to Si $_{0.66}$ Ge $_{0.34}$. (b) Series of (004) diffraction scans of the structure, where $\theta_{\rm B}$ is the Bragg angle. Two-axis geometry, full detector aperture, taken with a sealed-tube X-ray source (red); triple-axis geometry, Ge(222) channel-cut analyzer, using the same X-ray source (blue). The six thickest layers (and Si substrate) could be distinguished in the triple-axis case; the scan time was ~24 hrs. (c) Radial scan of same sample taken at beamline A with scan time of 15 min. Adapted from [22], with permission.

layer is deposited, the critical thickness is exceeded, and the layers start to relax. Figure 8(c) shows that layers 3, 4,

⁴ RADS, Bede Scientific Inc., Englewood, CO 80112.



Fiaure 7

(a) Ge-fraction profile for a series of step-graded $\mathrm{Si}_{1-x}\mathrm{Ge}_x$ structures grown on Si(001), each sample having an additional layer. (b) (004) radial scans of the same series of step-graded samples. The number of the diffraction peak corresponds to the layer number in (a). Adapted from [20], with permission.

and 5 were all partially relaxed. The mismatch strains at the start of the growth of layers 4 and 5 were found to be 0.0069 and 0.0083, respectively. Subsequent layers show mismatch strains at the start of their growth averaging around 0.006. Thus, once the layers start to relax, the mismatch strain always remains low and essentially constant. These strains are well within the range for the dislocation multiplication mechanism.

A number of other studies have been published using triple-axis diffraction at Port X20 on $Si_{1-x}Ge_x$ structures. The nucleation activation energy for the introduction of misfit dislocations was determined from the tilt angles

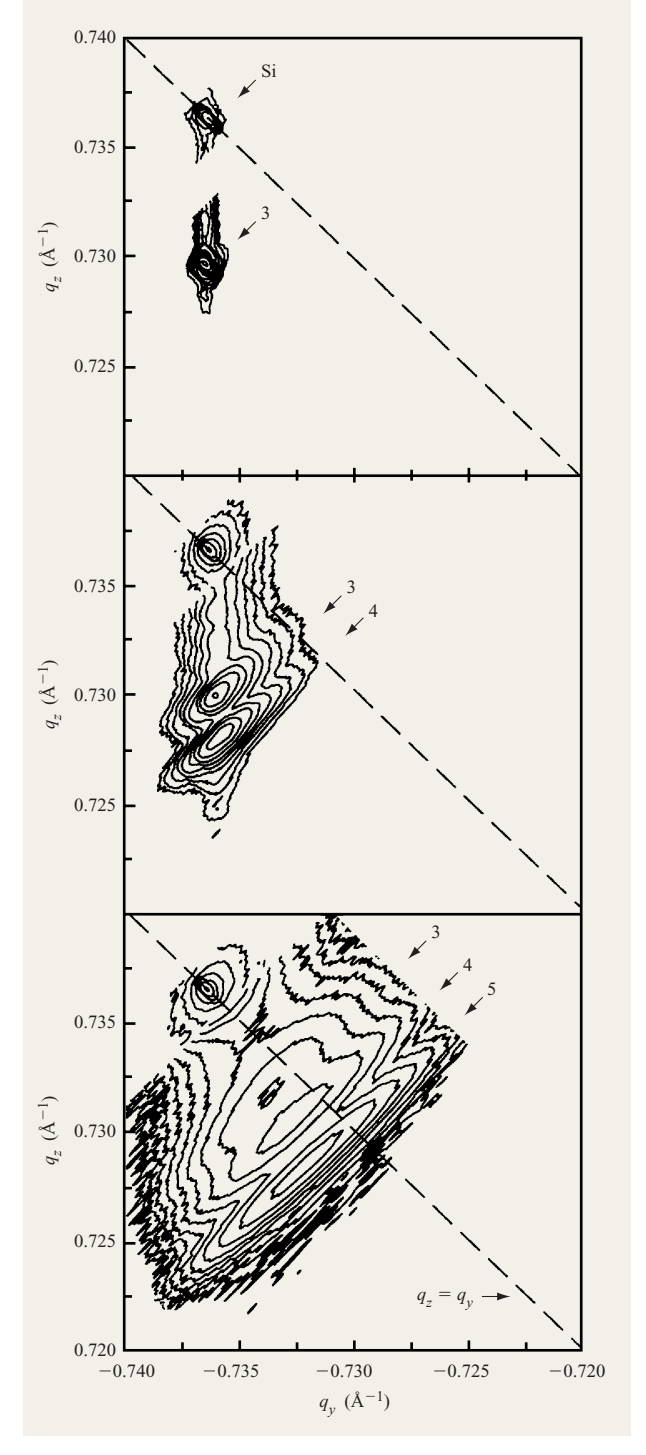
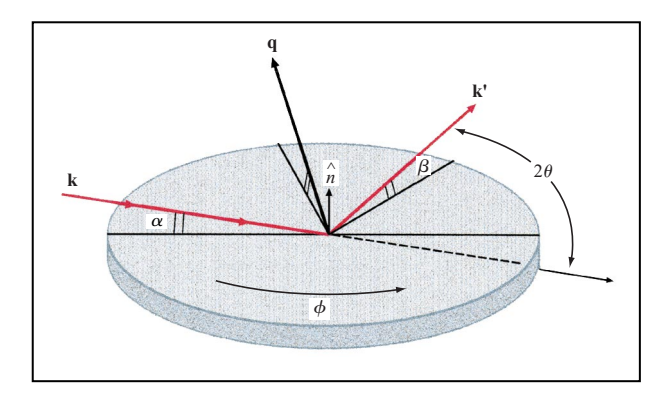


Figure 8

Reciprocal space maps in the Si(044) region of step-graded samples 3, 4, and 5. The iso-intensity contour lines are plotted on a log scale. The component q_z is inversely proportional to the out-of-plane lattice parameter, and q_y is inversely proportional to the in-plane lattice parameter. The peak numbers correspond to the layer numbers in Figure 7(a). Reprinted from [16], with permission.



Schematic of the geometric aspects of grazing-incidence diffraction. The grazing-incidence angle is α and the grazing exit angle is β . The scattering vector \mathbf{q} is the difference between the scattered and incident X-ray wave-vectors (\mathbf{k}' and \mathbf{k} , respectively) and has a magnitude of $(4\pi/\lambda)$ sin θ , where λ is the X-ray wavelength and θ is one half of the scattering angle 2θ . The surface normal is n, and ϕ is the rotation angle about the surface normal.

between various SiGe layers and a miscut Si(001) substrate [24]. A unique signature for the long misfit dislocations in very thin (\geq 360 Å) multiplication-relaxed films has been discovered using grazing-incidence reciprocal-space mapping [25]. The quality of Si_{1-x}Ge_x/Si heterostructures on sapphire substrates for application as *p*-channel FETs has been assessed [26]. Measurements also have been performed to evaluate several SiGe buffer-layer growth profiles for high-mobility FET devices [27].

Grazing-incidence diffraction: Near-surface ordering in polymers for flat-panel displays

In cases where one is interested in the structure of very thin films, standard diffraction methods may not yield useful data because of low signal strength or inaccurate determination of diffraction peak locations because of thickness broadening. Thickness broadening appears when only a limited number of unit cells are scattering coherently. For a small number of diffracting unit cells in the film thickness direction, z, scattering normal to the film surface is diffuse and broad. In grazing-incidence X-ray scattering (GIXS), the incident beam strikes the surface of the sample at a grazing angle, α , which is close to the critical angle, α_c (angle of total external reflection), for the material being measured. Diffracted rays are detected at a combination of an in-plane angle 2θ and an exit grazing angle β . Figure 9 illustrates the geometric aspects of GIXS. This technique is useful for measuring in-plane unit cell parameters and can be applied to adsorbed or freestanding films, crystal surfaces (reconstruction, roughening, or melting), depth profiling,

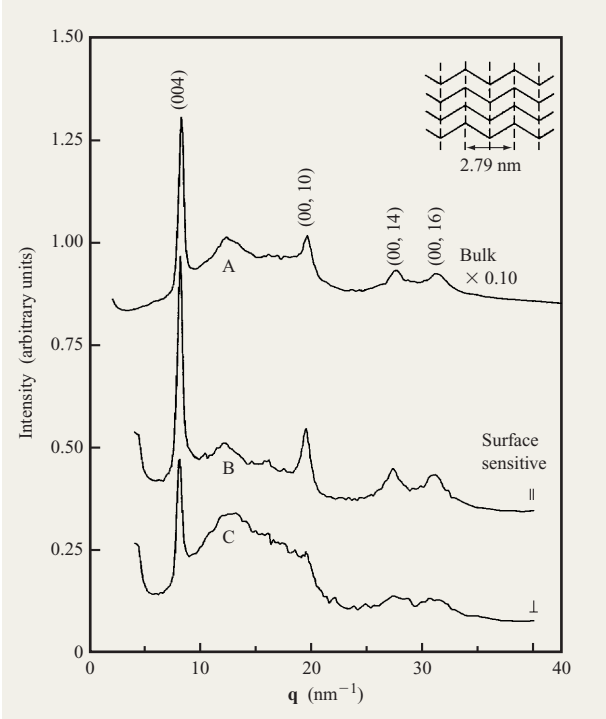
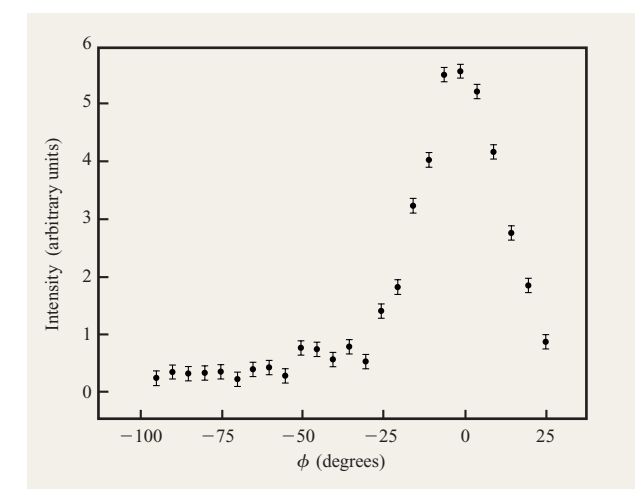


Figure 10

X-ray scattering intensity for a rubbed 200-nm-thick BPDA–PDA film imidized at 300°C. Curve A: Bulk-sensitive scan $(\alpha > \alpha_c)$ for ${\bf q}$ parallel to the rubbing direction. The bulk-sensitive scan $(\alpha > \alpha_c)$ for ${\bf q}$ perpendicular to the rubbing direction is identical. Curve B: Surface-sensitive scan $(\alpha = 0.25\,\alpha_c)$ for ${\bf q}$ parallel to the rubbing direction. Curve C: Surface-sensitive scan $(\alpha = 0.25\,\alpha_c)$ for ${\bf q}$ perpendicular to the rubbing direction. The data have been offset for clarity. The inset is a schematic representation of the structural ordering in BPDA–PDA. The dashed lines indicate the periodicity along the chain axis. Reprinted from [14], with permission.

etc. [28]. For the study described below, use was made of the multilayer monochromator on beamline C. High flux was needed to obtain reasonable diffraction intensities from a thin polymer film composed of the light elements C, H, O, and N.

GIXS has been used by M. F. Toney, T. P. Russell, and collaborators to obtain direct information on the near-surface structure of the polyimide films used to control the alignment of liquid crystals in flat-panel displays [14]. Buffing the polymer substrate films with a cloth produces liquid crystal alignment in the rubbing direction. Several possible explanations for this template effect have been postulated, including the generation of microgrooves or scratches and/or alignment of the polymer chains near the surface. **Figure 10** shows three diffraction scans for a rubbed 200-nm-thick BPDA-PDA film spun onto a Si(001) wafer and imidized at 300°C. The top scan was taken at an



Intensity of the rubbed BPDA–PDA film (004) peak as a function of the angle ϕ with respect to the rubbing direction. The data were recorded with the detector at a fixed 2θ while rotating ϕ . Reprinted from [14], with permission.

incident angle $\alpha > \alpha_c$, where X-rays penetrate the entire film. Scans taken with the scattering vector q both parallel and perpendicular to the rubbing direction were identical, and matched scans taken of unrubbed films. Thus, it was concluded that the bulk of the polyimide film was isotropic. The two lower scans were taken at grazing incidence ($\alpha = 0.25\alpha_s$), so that just the top ~ 5 nm of the sample was being probed. The scans for \mathbf{q}_{\parallel} vs. \mathbf{q}_{\perp} were distinctly different. The sharp Bragg peaks arising from the periodicity along the BPDA-PDA molecular axes [labeled (004), (0010), (0014), and (0016)] were significantly more intense for \mathbf{q}_{\parallel} than for \mathbf{q}_{\perp} . The broad reflections at $\mathbf{q} \approx 13$ and 30 nm⁻¹ were much stronger for \mathbf{q}_{\parallel} than for \mathbf{q}_{\parallel} . These arise primarily from intermolecular packing normal to the polymer chain axis. By comparing the (004) peak intensities, GIXS indicated that approximately twice as many chains in the surface region (≈ top 50 Å) are aligned parallel to the rubbing direction than are aligned perpendicular to it. These results show that the oriented polyimide chains act as a molecular template for liquid crystal alignment in flat-panel displays.

Scans taken of a 6-nm-thick rubbed film showed essentially complete alignment of chains along the rubbing direction. The angular spread of the aligned chains in the surface plane was determined by rotating the sample about an axis normal to the surface (ϕ -scan) while measuring the (004) peak intensity (**Figure 11**). Nearly all of the intensity occurred within $\pm 10^{\circ}$ of the buffing direction. The difference in amount of surface-region alignment between the 200-nm and 6-nm films indicated

that either $T_{\rm g}$ or the yield stress of the thinner film is lower than that of the near-surface region of the thicker film. This may be due to a lower "entanglement density," which would make the thin-film polymer chains more mobile.

Time-resolved diffraction: Phase transformations in titanium silicide contacts

Beamline C was designed as a high-flux beamline for the purpose of carrying out time-resolved X-ray diffraction studies [13]. One important component for such experiments is the monochromator. Using W-Si synthetic multilayers with a d-spacing of \sim 22 Å, two orders of magnitude more flux can pass through the monochromator than with S(111) or Ge(111). For a given energy of X-rays, as the *d*-spacing of diffracting planes increases, the Bragg angle decreases. If the Bragg angle is low enough, the reflected X-ray amplitude from each plane is significant, and extinction-limited diffraction occurs. The monochromator bandpass is inversely proportional to the number of planes that scatter coherently, similar to the situation of finite-thickness broadening. The energy spread of the multilayer monochromator used is $\Delta E/E \approx 1.2 \times 10^{-2}$.

The second important component of a time-resolved diffraction instrument is the ability to collect the diffracted intensities on the appropriately rapid time scale. Two detectors are in current use: a linear diode array which is an inch in length and intercepts $\sim 10^{\circ} \Delta 2\theta$ over 1024 pixels,⁵ and a CCD area detector which is 1 × 1 inch and has 1152 × 1242 pixels. The maximum speed of the linear detector is limited by the digitization rate; a 1024point scattering pattern can be taken every 17 ms and a grouped-pixel 64-point pattern requires 3 ms. This instrumentation was first developed to study the kinetics of phase separation and ordering in binary alloys such as the Al-Zn system and Cu₂Au [13, 29]. It also has proven to be extremely valuable for studying a number of materials systems important to the CMOS and DRAM processes used by IBM. Knowledge and control of the behavior of materials as they undergo processing steps in the manufacture of chips is vital to the success of each new generation of device. On beamline C, phase transformations, intermixing of materials, and texture evolution can be studied in situ and in real time during rapid thermal annealing (RTA).

The third vital component for these time-resolved studies is precise control of sample temperature over the time resolution desired. A unique chamber and "furnace" have been designed that can ramp small samples up in temperature to 1200° C at a rate of $\leq 35^{\circ}$ C/s in vacuum or an inert atmosphere [30]. Samples can be quickly

⁵ Princeton Instruments XPDA-1024 detector head and ST-1000 controller.

⁶ Princeton Instruments LCX-TE/CCD-1242EHR detector head and ST-138

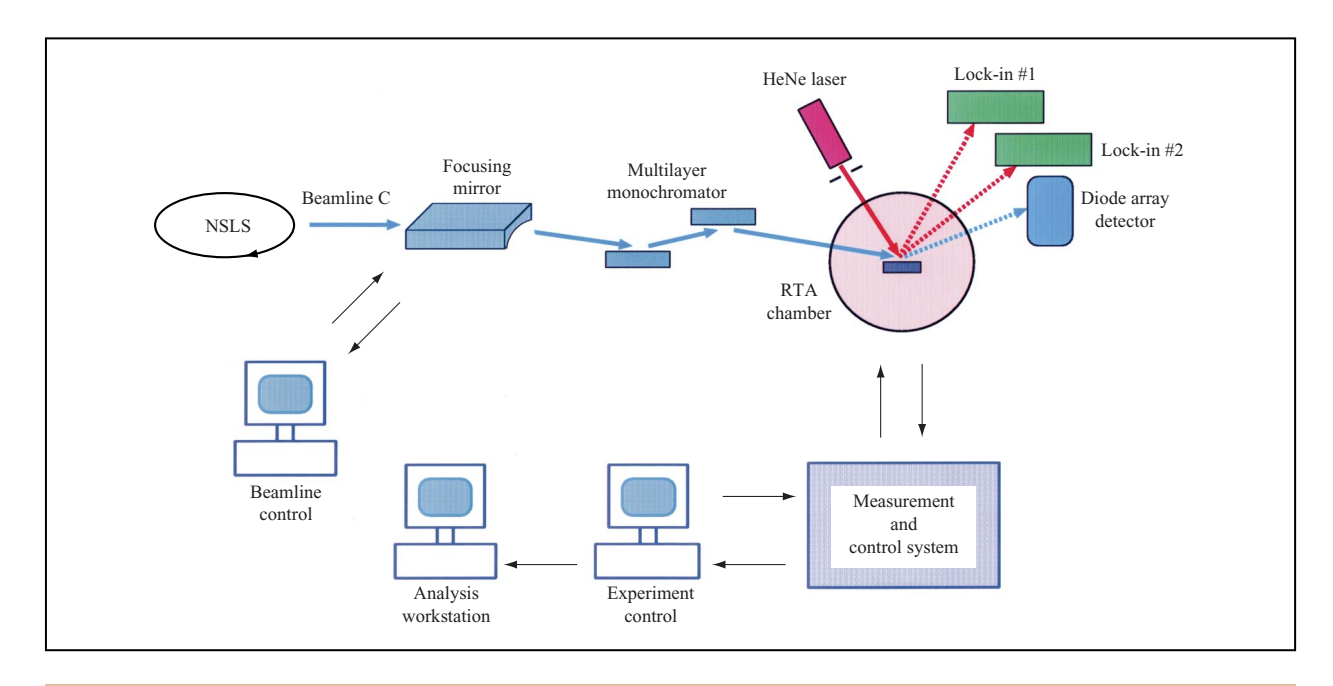


Figure 12

Schematic of the three-probe configuration at beamline C for time-resolved diffraction from metal silicides.

quenched to room temperature in order to freeze in an interesting phase for more detailed ex situ analysis. In addition to X-ray diffraction, the chamber also is equipped to provide, in real time, four-point resistance measurements of a sample and optical-wavelength elastic light scattering from the surface of the sample [31]. A HeNe laser provides light which passes through fiber optic cables into the chamber and strikes the sample at $\alpha=25^\circ$. Light scattered at -21° and 52° with respect to the surface normal is collected by a fiber optics system and sent to photodiodes. Scattered light from the two angles is sensitive to surface morphologies on lateral length scales of $\sim 0.5~\mu m$ and $\sim 5.0~\mu m$, respectively. A schematic of beamline C configured for three-probe time-resolved studies is shown in Figure 12.

Metal silicides are used as contacts on sources, gates, and drains of MOSFETs and for interconnections in logic and memory devices. TiSi₂ has been the material of choice for past and current generations of CMOS circuits because of its low resistivity and good thermal stability [32]. Unfortunately, it exhibits a bimodal contact resistance when formed on small features, behavior that wreaks havoc on the timing structure of signals in a circuit [33]. In the SAlicide (Self-Aligned salicidation) process (Figure 13), Ti is deposited onto a wafer and reacts with exposed silicon on gates, sources, and drains during a formation anneal at ~700°C for 20 s. A base-centered orthorhombic phase of TiSi, is formed (C49) that has a high resistivity

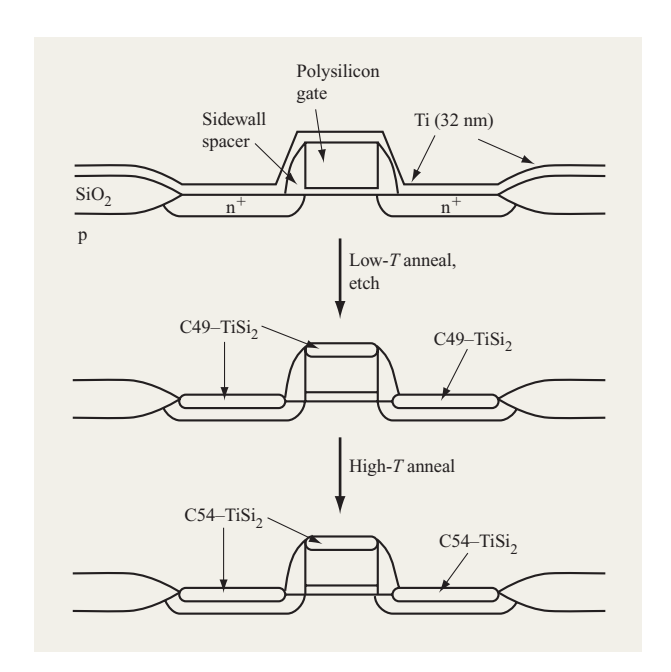


Figure 13

Schematic of the SAlicide process for producing titanium disilicide contacts on MOSFET source, gate, and drain regions.

of ${\sim}60$ –90 ${\mu}\Omega$ -cm. After unreacted Ti is etched away from SiO₂ and Si₃N₄ spacer regions, a transformation

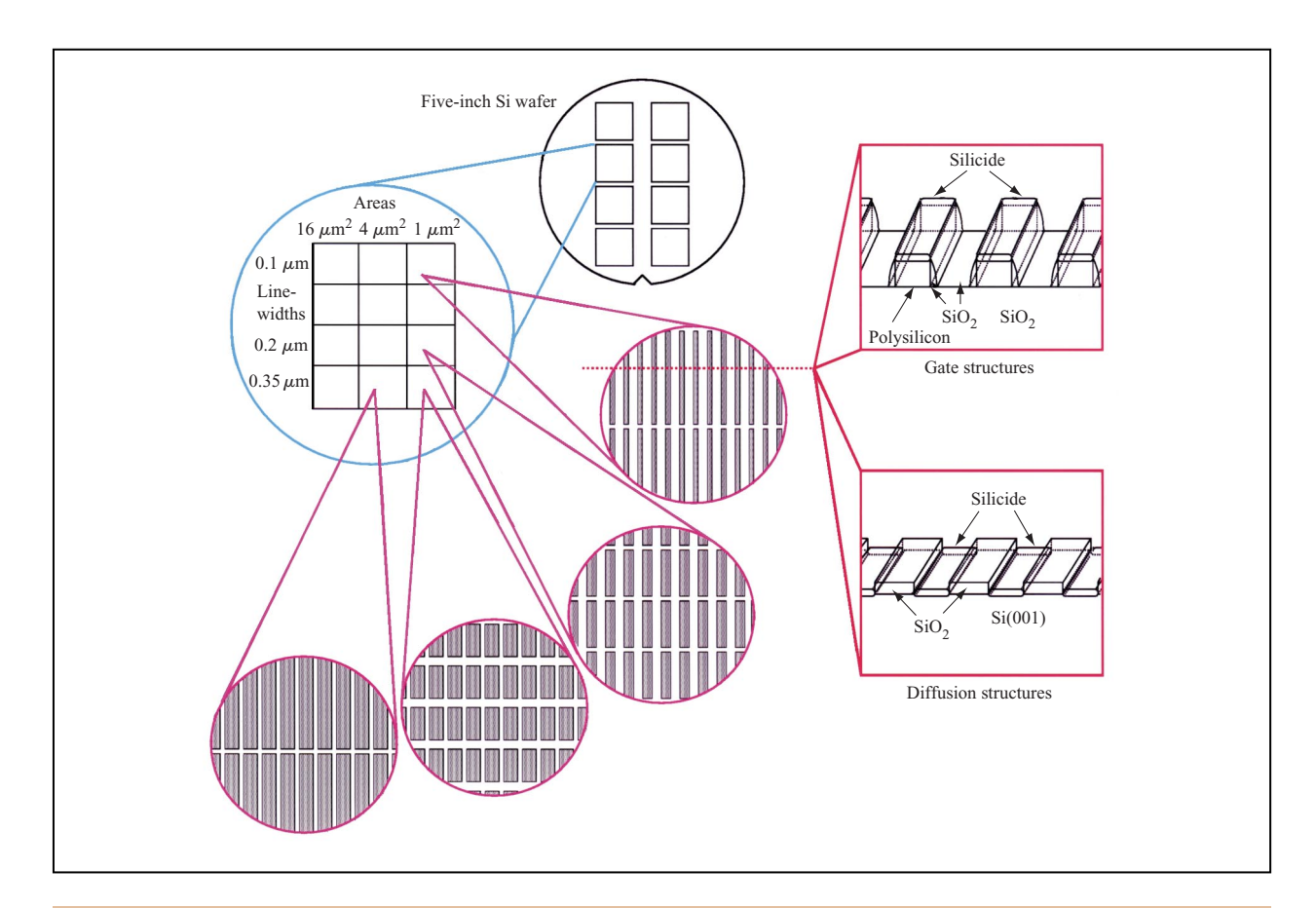


Figure 14

Schematic of the test sites used for time-resolved diffraction studies of metal silicides.

anneal above 800°C converts the C49 TiSi_2 to a face-centered polymorph called C54, which has a resistivity of \sim 12–20 $\mu\Omega$ -cm. It is untransformed C49 that causes the bimodal behavior, and the transformation from C49 to C54 TiSi_2 requires more heat as the widths of narrow silicide lines decrease [34]. This requirement for higher temperatures or longer heating times is detrimental to the narrow processing window required for ULSI.

The behavior of TiSi₂ formation as a function of RTA ramp rates, endpoint temperatures, substrate type and doping, contact area, and aspect ratio has been studied extensively at beamline C by members of J. M. E. Harper's group and their collaborators. There are several advantages to using time-resolved, *in situ* diffraction for these studies, rather than the more conventional electrical testing or postannealing X-ray diffraction [30]. It is extremely efficient. A sample can be mounted and measured, and data collected and processed for the entire temperature range in about 15 minutes. Hundreds of samples can be measured during an experimental run.

Thus, the effect of variations in many parameters can be studied exhaustively. In ex situ electrical testing only one feature is measured at a time, and the large contact probes have been shown to affect the results of the measurement [35]. However, the diffraction measurements are statistically meaningful and free from this and other artifacts because the X-ray beam probes a sample containing hundreds of thousands of isolated, identical features. The transformation can be followed continuously in real time, so that the exact temperature of transformation is always obtained, and interesting phases can be noted and "frozen in" by thermal quenching for subsequent ex situ analysis [30]. Samples consist of either blanket films or test sites that simulate gates, or sources, drains, and interconnects. Figure 14 shows a schematic of these test sites and two types of experimental structures. Each sample was \sim 4 mm \times 7 mm in area and contained an array of identical line or segmented line structures. The linewidths varied from 0.1 μ m to 1.0 μ m and the areas varied from 1 μ m² to 25 μ m².

468

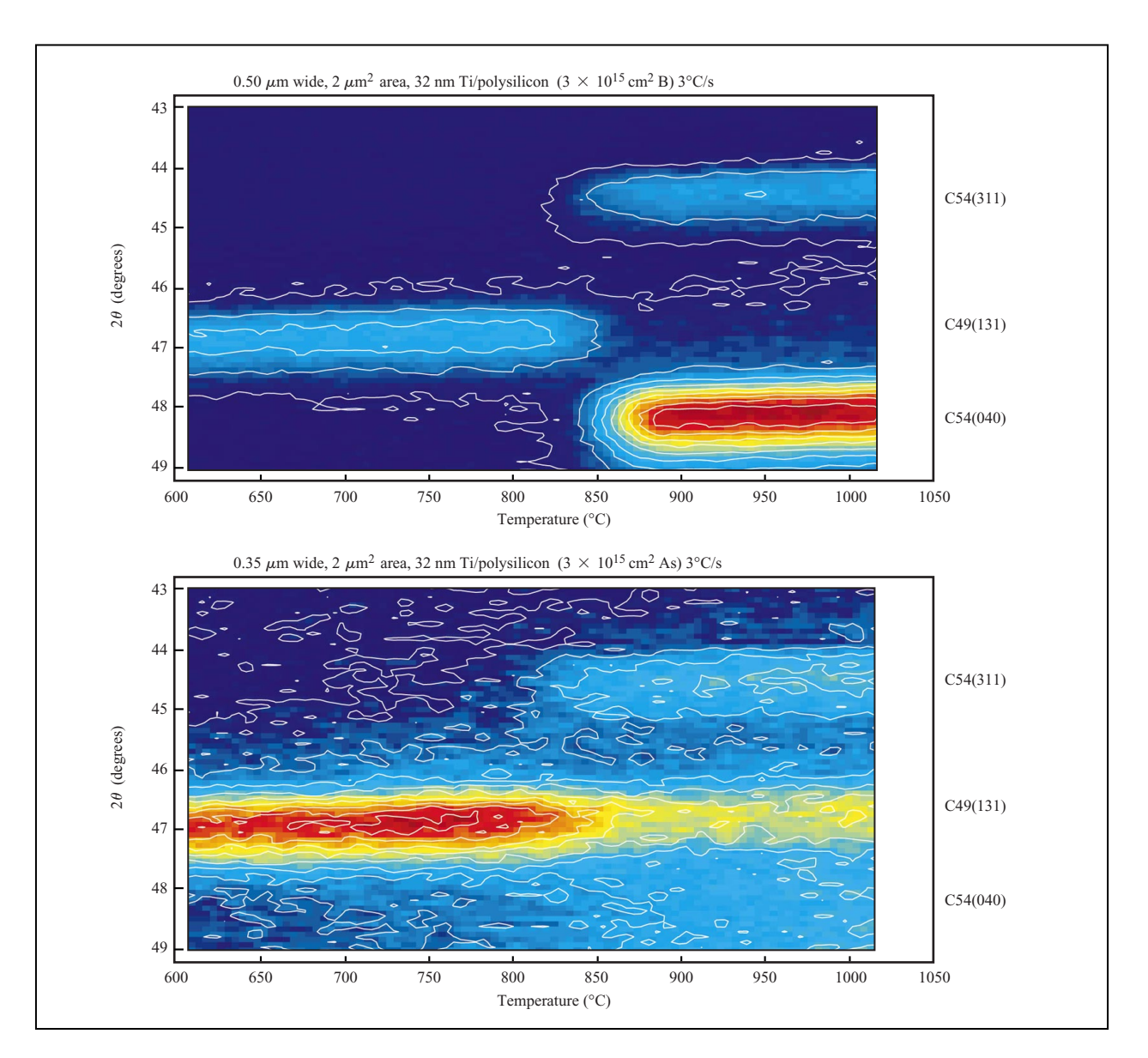


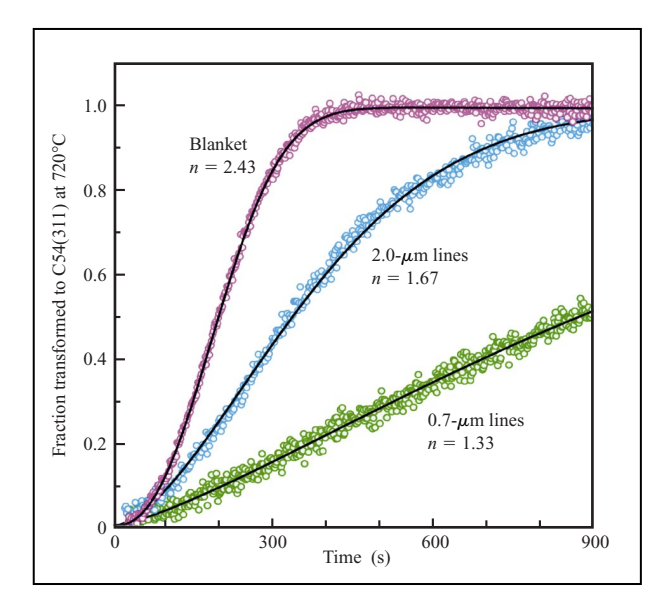
Figure 15

Diffracted X-ray intensity contours for $\Delta 10^{\circ}2\theta$ measured by a linear diode array detector as a function of sample temperature. The samples were ramped from 100 to 1020 °C at 3 °C/s. The top contour map is for an array of 2- μ m² contact areas, 0.5 μ m wide. The lower contour map is for an array of 2- μ m² contact areas, 0.35 μ m wide. One can see indications of untransformed C49 in the lower sample.

For the study of $TiSi_2$ phase transformations, an X-ray energy of 6.9 keV was used, and the center pixel of the linear diode array was set at $2\theta=45^\circ$. Over an angular spread of 10° $\Delta 2\theta$, diffracted intensity from the Ti(002), $C49-TiSi_2(131)$, $C54-TiSi_2(311)$, and $C54-TiSi_2(040)$ reflections was collected. Series of 2θ traces were taken every 0.5 s for samples ramped from 600°C to 1020° C at a rate of 3° C/s under a nitrogen atmosphere. Two series are shown in **Figure 15** as contour maps of diffracted X-ray

intensity. Red and blue represent high and low intensity, respectively. The top sample consisted of arrays of 0.50- μ m-wide gate contact structures, 2 μ m² in area, formed by deposition of a 32-nm Ti film on a polysilicon substrate doped with a boron dose of 4 \times 10¹⁵/cm² at 40 keV. The patterned samples were typically annealed to form the C49-TiSi₂ and etched before the time-resolved analysis. The maximum increase in slope for the integrated intensity over the C54-TiSi₂(040) region of interest yields

469



Isothermal transformation curves taken at 720°C for a 32-nm Ti blanket film on Si(001), and for $2.0-\mu$ m-wide lines and $0.7-\mu$ m-wide lines of the same film. The fraction of C49 converted to C54(311) is plotted vs. time. The black lines are fits to the data, and n is the value of the Avrami exponent for each curve.

the transformation temperature. The lower sample was an array of narrower, 0.35- μ m-wide structures, $2 \mu m^2$ in area, and doped with 3×10^{15} /cm² As at 35 keV. It is clear that the narrower-linewidth structures do not fully transform to C54 TiSi,, even up to 1020°C. The fraction of C49 transformed into C54 at a given temperature is $[I_{\text{C54(040)}} + I_{\text{C54(311)}}]/[I_{\text{C49(131)}} + I_{\text{C54(040)}} + I_{\text{C54(311)}}], \text{ where}$ I is the integrated area under the designated diffraction peak at that temperature. Transformation temperatures and fractions transformed were measured for a series of samples of constant area $(2 \mu m^2)$, ranging in linewidth from 0.1 to 0.35 μ m (see footnote 7). Each sample had about half a million identical gate structures probed by the X-ray beam. For arsenic-doped (3×10^{15}) cm² at 35 keV) structures, the transformation temperature increased from 855°C to 904°C with decreasing linewidth. For borondoped $(4 \times 10^{15}/\text{cm}^2 \text{ at } 40 \text{ keV})$ structures, the transformation temperature increased from 879°C to 949°C. For both types of dopant, the fraction transformed by 1025°C ranged from 50% down to 38% with decreasing linewidth. None of these small-area structure samples underwent complete transformation to the C54 polymorph. Another set of samples having constant linewidth (0.2 μ m) and areas varying from 25 μ m² down to 1 μ m² was

also measured. Arsenic-doped samples displayed transformation temperatures that increased from 822°C to 1010°C with decreasing area. Boron-doped sample temperatures increased from 820°C to 960°C. The fraction transformed to C54 was strongly dependent upon area, independent of dopant. Areas of 12 $\mu \rm m^2$ and higher underwent complete transformation. Below 12 $\mu \rm m^2$, the fraction transformed decreased rapidly, down to $\sim\!25\%$ for 0.1- $\mu \rm m^2$ structures.

Kinetic studies have been carried out by maintaining samples at an elevated temperature and recording the evolution of C54 peaks over time. The resultant sigmoidal curves showed typical incubation, rapid growth, and saturation, and were fit using Johnson-Mehl-Avrami analysis [36]. Three of these "isothermal" curves are shown in Figure 16. As can be seen, the blanket film transformed much more rapidly than the 2- μ m- or 0.7- μ mwide lines; the narrower lines must be elevated to higher temperatures to obtain complete transformation. From the analysis, the Avrami exponent and activation energy were obtained [36] for the C54 nucleation, which usually occurs at C49 triple-grain boundaries [37]. From the Avrami exponent one can derive information about nucleation and growth, as well as about the dimensionality of the transformation. For blanket films and lines (independent of width), the activation energy for the nucleation of C54 has been found to be \sim 4 eV (see footnote 8).

The behavior of these structures can be explained qualitatively by a model in which, for small-area features, the nucleation site density is small enough that not all features contain a site. Those features then would not undergo transformation. In narrow lines, the growth is one-dimensional because of the boundary constraints of the sides of the lines. A crossover from 1D to 2D growth occurs at a critical linewidth, which depends upon C54 nucleation site density [30]. For samples studied, the nucleation density was $<0.3/\mu m^2$ (see footnote 8), and the crossover width was below 1 μm .

The ion implantation of a small dose of Mo into the silicon before deposition of Ti lowers the transformation temperature by 100–150°C and makes the complete transformation less dependent upon structure geometry [38]. The addition of an intermediate Mo layer between the Ti and Si has the same effect [39]. A series of experiments were performed by C. Cabral, Jr., and coworkers to test the transformation behavior and contact quality of a series of Ti alloys of varying concentration [40]. The lowest resistivities and transformation temperatures down to 715°C were obtained for blanket films with less than 10 at.% Ta or Nb. For isolated

⁷ L. A. Clevenger, C. Cabral, Jr., C. Lavoie, R. A. Roy, V. Svilan, R. Vaswanathan, K. L. Saenger, A. Pomerene, J. Jordan-Sweet, G. Morales, and K. L. Ludwig, Jr., uppublished work

⁸ G. B. Stephenson and L. A. Clevenger, unpublished work.

submicron Ti(Ta) alloy structures on Si(001) and polysilicon, the temperature at which the C49-C54 phase transformation takes place was reduced to less than 900°C. Figure 17 shows the effect of Ti(Ta) alloys on the transformation temperatures and fraction transformed for submicron gate structures (polysilicon) as a function of linewidth. This improvement allows for C54 formation before the onset of thermal degradation. It has been postulated that all of these improvements arise because of an increase in the nucleation-site density through the formation of smaller C49 grains [38]. Cabral et al. also discovered the appearance of a Ti(alloy)Si, C40 phase (in agreement with other Mo interlayer studies [41]). MoSi, TaSi,, and NbSi, all have C40 "CrSi,"-type structures which are similar enough to C54 to possibly provide a template effect for the nucleation of C54 grains [40].

Some of these improvements have been incorporated into device-processing technology at IBM. The time-resolved instrumentation at X20C has been used for a number of other applications, including CoSi₂ formation [42], NiSi formation, intermetallic mixing and phase formation, and diffusion barrier studies.

Microdiffraction: Strain fields in Ni/Si structures

Recently a special-purpose instrument was commissioned by I. C. Noyan and coworkers [43–45] involving the use of micron-sized X-ray beams to investigate technological issues related to structure and strain in small features. Some of these issues include thermally and electrically induced failure in thin metal lines [46], defect fields in heteroepitaxial films [47], and interfacial strain in small metal features deposited on silicon due to thermal expansion mismatch [43–45, 48]. Problems such as these require high-brightness X-rays in order to obtain enough signal from the region of interest and to avoid unwanted signals from surrounding areas.

The microdiffraction apparatus used consists of a microfocusing tapered glass capillary and 0.5- μ m-resolution x, y, and z sample-scanning stages mounted on a standard two-circle Huber diffractometer with partial χ and ϕ arcs. The capillary accepts the incident X-ray beam and condenses it into a spot several microns in diameter just in front of the sample. A photograph of the capillary (thin glass tube at the center of the photograph) and sample stage is shown in **Figure 18**. The χ and ϕ arcs are mounted on translators so that all of the diffractometer circles can be adjusted carefully to bring them into concentricity. Despite this, the "sphere of confusion" of the diffractometer cannot be reduced mechanically to less than tens of microns. Accordingly, a protocol for measuring and compensating for the ω , χ , and ϕ radii of

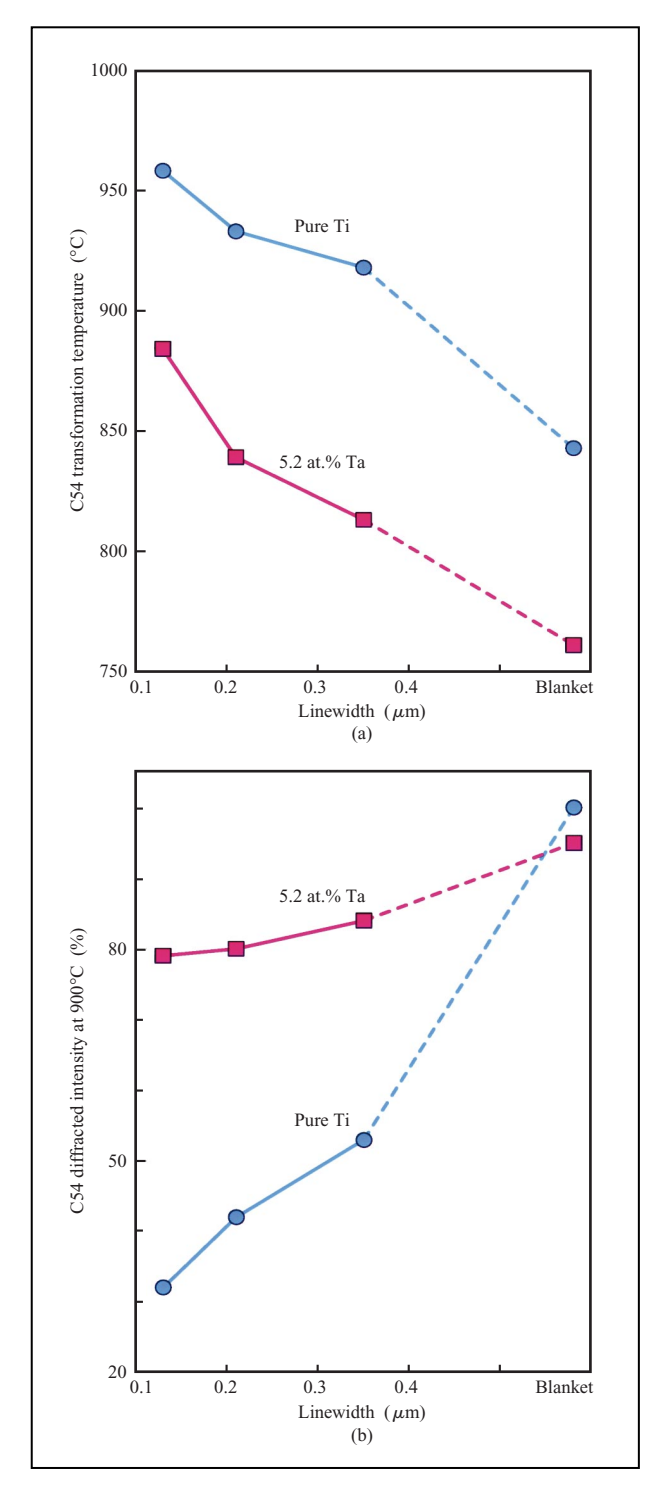


Figure 17

C54 $TiSi_2$ phase transformation temperature (a) and percent transformed from C49 (b), each as a function of linewidth for submicron isolated features metallized with 31 nm of Ti or 34 nm of Ti(5.2 at.% Ta) on polycrystalline Si. Samples were annealed at a ramp rate of 3°C/s up to 1025°C in N_2 . Adapted from [40], with permission.

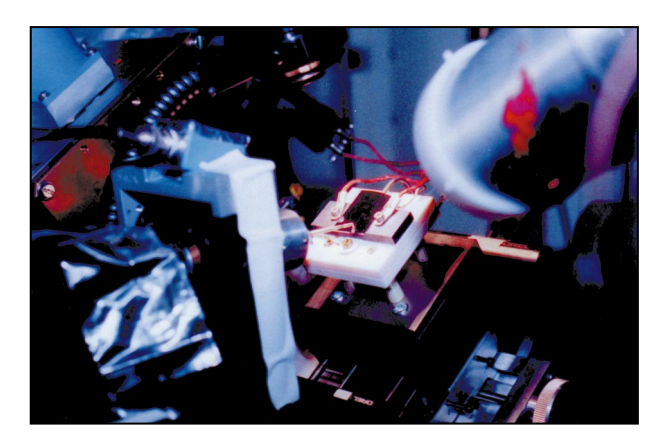


Figure 18

Photograph of capillary (center) and sample stage of microdiffraction system. The capillary is directed toward a Si wafer mounted on the sample stage.

confusion has been developed [49]. This is essential in cases where several diffraction peaks are to be measured at a specific location on the sample.

The capillaries used are fabricated in-house⁹ and have inner surfaces tapered to approximate a parabola so that X-rays undergo several total external reflections off the inside walls and converge at a critical angle of $\sim 0.3^{\circ}$. Precise alignment is crucial, and the capillary used is mounted in a gimbal having two rotational and three translational degrees of freedom. The focus of the X-ray beam is extremely close to the tip of the capillary. The divergence and spot size have been measured by knifeedge scans to be $\sim 0.35^{\circ}$ and from 2 to 20 μ m in diameter, respectively. The FWHM of the X-ray beam from our "best" capillary, at a typical sample distance of 1.4 mm from the tip, is $\sim 3 \mu m$, and the flux at 8.5 keV is $\sim 1.5 \times 10^8$ cts/s. The actual footprint of the beam on the sample increases as sin ω , where usually $\omega = 2\theta/2$ for the diffraction peak being measured.

The instrument has three modes of operation. One is diffraction imaging (microtopography), in which the detector is moved to a reflection of interest, and the diffracted intensity is collected as the sample is rastered in the beam. This mode is used for grain mapping, defect imaging, strain contrast mapping, etc. Once a "mesh" has been made across a submillimeter-sized area, one can return easily to regions of high intensity and "tweak" them up, in preparation for more detailed measurement of lattice tilt, mosaic broadening, or lattice spacing. This is

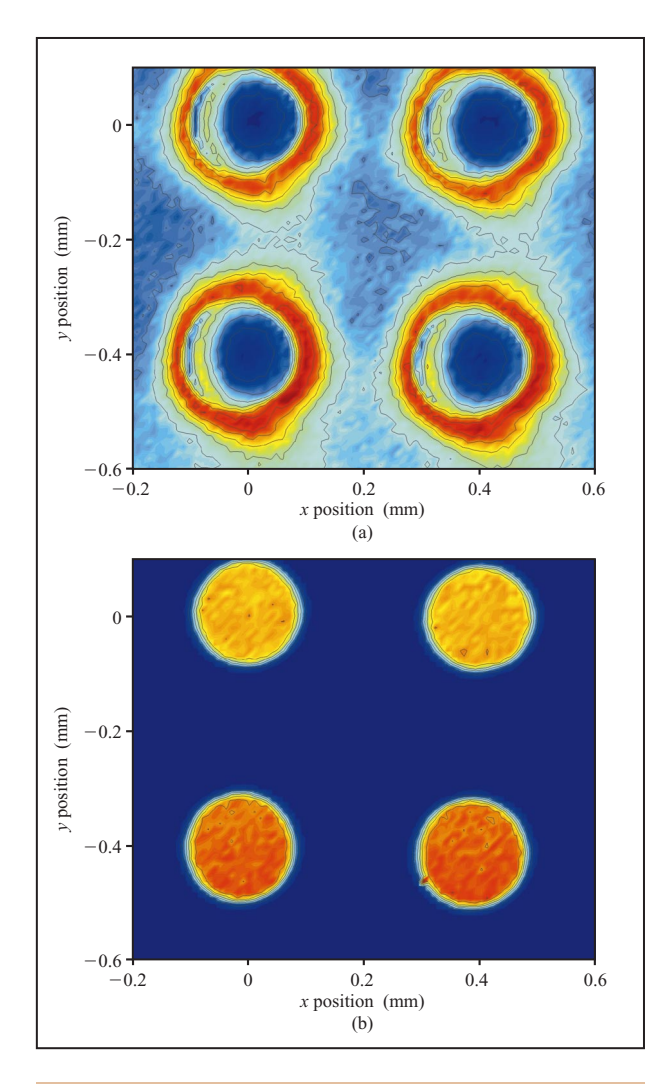
the second mode: standard diffraction analysis. For a silicon wafer at the Si(004) reflection angle of 32° θ (at 8.5 keV) the measured d-spacing repeatability is $\Delta d/d = 0.0003$ [50]. The third mode of operation is fluorescence mapping, for which the sample again is translated in the beam and the fluorescence signal of interest is collected by a Si(Li) energy-dispersive detector. This is useful for mapping fluorescence markers or other features for alignment of the sample in the X-ray beam, for measuring the sphere of confusion of the diffractometer, and for measuring the electromigration material along a line.

A recent illustration of the capabilities of this instrument (one that yielded unexpected results) was the study of interfacial strain caused by residual stresses in small Ni metallization features deposited on Si(111) [48]. In discrete thin-film features, the feature edges cause significant shear stresses/strains, unlike blanket films, in which the stresses are biaxial and isotropic. The sample in this study consisted of an array of 190-µm-diameter Ni pads, 1 μ m thick, separated by 220 μ m, deposited by vacuum evaporation onto a Si(111) substrate maintained at room temperature. To characterize the strain distribution, the Si(333) integrated diffraction intensity was mapped by step-scanning over an area containing several pads. Simultaneously, the Ni K α fluorescence signal at 7.478 keV was recorded using a Si(Li) detector. The X-ray spot on the sample was an ellipse 14 µm in the direction parallel to the diffraction plane and 10 μ m normal to it. Figure 19 shows contoured area maps of the Si(333) diffraction intensity and Ni fluorescence intensity. Part (a) is essentially a strain map of the Si substrate. When unperturbed, diffraction from a silicon substrate is dynamical and is limited by extinction effects [51]. When the silicon lattice is strained, it becomes imperfect, extinction effects are eliminated, and the diffracted intensity increases. The smooth blue regions correspond to relatively strain-free Si under or close to the Ni pads. The lack of intensity fluctuations under the pad demonstrated that the adhesion was uniform and good. The contours outside the pads correspond to the far-field strains induced in bare Si by the Ni, which appeared to be circularly symmetric. Comparison with part (b) indicates that the strain field was much larger than the pad diameter. Figure 20 shows a close-up profile scan across one pad. The blue circles corresponding to the diffraction intensity reached a maximum outside the edge of the fluorescence intensity (red circles). This surprising result showed that the position of maximum strain contrast is $\sim 20 \mu m$ outside the edge of the Ni pad, contrary to results from analytical solutions and finite-element models of interfacial strain. Work is in progress on comparing the stress/strain transfer between a variety of metal film structures and silicon substrates, including Al [43-45], W, and Cu.

 $^{^{9}}$ E. G. Liniger of the IBM Research Division manufactures the capillaries used at X20.

Summary

Examples have been shown to illustrate the wide range of materials that can be studied and measurements that can be made using diffraction principles and the extremely intense source of X-rays provided by the National Synchrotron Light Source. A number of groups throughout IBM, primarily from the Research Division, utilize the beamlines at Port X20 to extend the information they gather in their microelectronics technology efforts. The projects range from having near-term impact, such as the TiSi₂ work, to furthering the understanding of materials-related phenomena that pertain to potential applications.



Fiaure 19

Equi-intensity contour plots for Si(333) diffraction (a) and Ni–K α fluorescence (b) over a 0.8-mm \times 0.7-mm area on a sample containing four Ni pads. The step size used in the raster scan was 10 μ m in both directions. The isointensity contours indicate regions of constant strain. Adapted from [48], with permission.

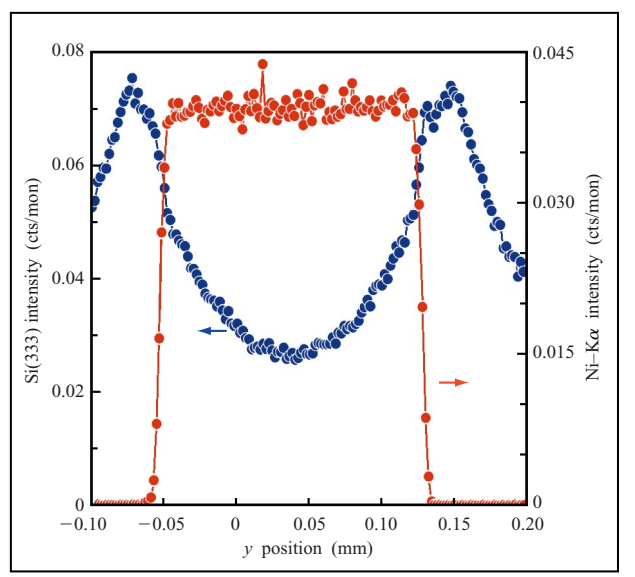


Figure 20

Intensity variation across one Ni pad for Si(333) diffraction and Ni–K α fluorescence, as shown respectively by red and blue circles. The intensities were normalized to the monitor counts, and the step size used was 2 μ m. Adapted from [48], with permission.

Acknowledgments

I wish to thank all of the collaborators I have had over the years at IBM and at the National Synchrotron Light Source, and the many people who have generously shared with me their knowledge of instrumentation, X-ray optics, techniques, etc. In particular, I thank Brian Stephenson, Pat Mooney, Mike Toney, Cev Noyan, Larry Clevenger, Cyril Cabral, Jr., Christian Lavoie, Carol Thompson, and Ken Evans-Lutterodt. I also acknowledge the vital assistance of our Port X20 beamline specialists over the years: Joe Peidle, Rene Holaday, and Steve LaMarra, who have run things so competently that I can spend significant time on research projects. The National Synchrotron Light Source at Brookhaven National Laboratory is supported by DOE Contract No. DE-AC02-76CH00016.

*Trademark or registered trademark of International Business Machines Corporation.

**Trademark or registered trademark of The Open Group or X/Open Company Ltd.

References and notes

 A. L. Robinson, "Third-Generation Synchrotron Light Sources," *Beam Line*, Spring 1994, pp. 17–27; R. E. Watson and M. L. Perlman, "Seeing with a New Light: Synchrotron Radiation," *Science* 199, 1295–1302 (1978).

- W. Brefeld and P. Gurtler, "Synchrotron Radiation Sources," *Handbook on Synchrotron Radiation*, S. Ebashi, M. Koch, and E. Rubenstein, Eds., Elsevier Science, Holland, 1991, pp. 269–296.
- 3. H. Winick, "Synchrotron Radiation," Sci. Amer. **257**, No. 5, 88–99 (1987).
- 4. J.-L. Laclare, "Conclusions for the 10th ICFA Workshop, January 1996," *ESRF Newsletter*, March 1996, pp. 6–7.
- G. P. Williams, editorial, Synchrotron Radiation News 10, No. 1, 2–3 (1997); A. E. Brenner, "The Computing Revolution and the Physics Community," Phys. Today, October 1996, pp. 24–30.
- Synchrotron Radiation News, The Gordon and Breach Publishing Group, P.O. Box 32160, Newark, NJ 07102; Journal of Synchrotron Radiation, Munksgaard International Publishers, 35 Norre Sogade, P.O. Box 2148, DK-1016, Copenhagen K, Denmark.
- 7. "Research by Industry at the National Synchrotron Light Source," Report No. BNL-61553, Brookhaven National Laboratory, Upton, NY, May 1995; D. L. White, J. E. Bjorkholm, J. Bokor, L. Eichner, R. R. Freeman, T. E. Jewell, W. M. Mansfield, A. A. MacDowell, L. H. Szeto, T. W. Taylor, D. M. Tenant, W. K. Waskiewicz, D. L. Windt, and O. R. Wood II, "Soft X-Ray Projection Lithography," Solid State Technol. 34, 37 (1991); J. B. Murphy, D. L. White, and A. A. MacDowell, "Synchrotron Radiation Sources and Condensers for Projection X-Ray Lithography," Appl. Opt. 32, 6920–6929 (1993).
- "Imaging Research at the National Synchrotron Light Source," Report No. BNL-45765, Brookhaven National Laboratory, Upton, NY, 1990; J. Warlaumont, "X-Ray Lithography: On the Path to Manufacturing," J. Vac. Sci. Technol. B 7, No. 6, 1634–1641 (1989); A. D. Wilson, "X-Ray Lithography in IBM, 1980–1992, the Development Years," IBM J. Res. Develop. 37, No. 3, 299–318 (1993).
- P. Pianetta, N. Takaura, S. Brennan, W. Tompkins, S. S. Laderman, A. Fischer-Colbrie, M. Madden, D. C. Wherry, and J. B. Kortright, "Total Reflection X-Ray Fluorescence Spectroscopy Using Synchrotron Radiation for Wafer Surface Trace Impurity Analysis," Rev. Sci. Instrum. 66, No. 2, 1293–1297 (1995).
- S. L. Hulbert and G. P. Williams, "New Experimental Facilities at the National Synchrotron Light Source VUV Ring," Synchr. Rad. News 10, No. 1, 16–21 (1997).
- R. P. Haelbich, J. P. Silverman, and J. M. Warlaumont, "Synchrotron Radiation X-Ray Lithography," *Nucl. Instr. Meth. Phys. Res. A* 222, 291–301 (1984).
- 12. B. D. Cullity, *Elements of X-Ray Diffraction*, 2nd ed., Addison-Wesley Publishing Co., Reading, MA, 1978, pp. 86–87.
- G. B. Stephenson, "Time-Resolved X-Ray Scattering Using a High-Intensity Multilayer Monochromator," Nucl. Instr. Meth. Phys. Res. A 266, 447–451 (1988).
- M. F. Toney, T. P. Russell, J. A. Logan, H. Kikuchi, J. M. Sands, and S. K. Kumar, "Near-Surface Alignment of Polymers in Rubbed Films," *Nature* 374, 709–711 (1995).
- B. S. Meyerson, D. L. Harame, J. Stork, E. Crabbé, J. Comfort, and G. Patton, "Silicon:Germanium Heterojunction Bipolar Transistors: From Experiment to Technology," *Intl. J. High Speed Electron. Syst.* 5, No. 3, 473–491 (1994); B. S. Meyerson, "High-Speed Silicon-Germanium Electronics," *Sci. Amer.* 270, No. 3, 62–67 (1994).
- P. M. Mooney, "Strain Relaxation and Dislocations in SiGe/Si Structures," *Mater. Sci. & Eng. Rep.* R17, 105–146 (1996); P. M. Mooney and J. L. Jordan-Sweet, "High Resolution X-Ray Diffraction Applied to Strain Relaxation of Lattice Mismatched Semiconductor Films," *Adv. X-Ray Anal.* 41 (CD-ROM) (ICDD, Newton Square, PA, 1999).

- 17. Below the critical thickness, a pseudoepitaxial film is fully strained, and the system does not have enough energy to form the defects needed to relax. Above the critical thickness, the film can relax to its natural lattice constant; J. Matthews and A. Blakeslee, "Defects in Epitaxial Multilayers," *J. Cryst. Growth* 27, 118–125 (1974).
- J. Tersoff and F. K. LeGoues, "Competing Relaxation Mechanism in Strained Layers," *Phys. Rev. Lett.* 72, 3570–3573 (1994).
- F. K. LeGoues, B. S. Meyerson, and J. F. Morar, "Anomalous Strain Relaxation in SiGe Thin Films and Superlattices," *Phys. Rev. Lett.* 66, 2903–2906 (1991); F. K. LeGoues, B. S. Meyerson, J. F. Morar, and P. D. Kirchner, "Mechanism and Conditions for Anomalous Strain Relaxation in Graded Thin Films and Superlattices," *J. Appl. Phys.* 71, No. 9, 4230–4243 (1992); K. W. Schwarz, "Interaction of Dislocations on Crossed Glide Planes in a Strained Epitaxial Layer," *Phys. Rev. Lett.* 78, 4785–4788 (1997); K. W. Schwarz and F. K. LeGoues, "Dislocation Patterns in Strained Layers from Sources on Parallel Glide Planes," *Phys. Rev. Lett.* 79, 1877–1880 (1997).
- P. M. Mooney, J. L. Jordan-Sweet, J. O. Chu, and F. K. LeGoues, "Evolution of Strain Relaxation in Step-Graded SiGe/Si Structures," *Appl. Phys. Lett.* 66, 3642–3644 (1995).
- P. F. Fewster, "X-Ray Diffraction from Low-Dimensional Structures," Semicond. Sci. Technol. 8, 1915–1934 (1993).
- P. M. Mooney, J. L. Jordan-Sweet, G. B. Stephenson, F. K. LeGoues, and J. O. Chu, "High Resolution X-Ray Diffraction Measurements of Strain Relaxed SiGe/Si Structures," Adv. X-Ray Anal. 38, 181–183 (1995).
- J. L. Jordan-Sweet, P. M. Mooney, and G. B. Stephenson, "High-Resolution X-Ray Diffraction Measurements of SiGe/Si Structures," *Mater. Res. Soc. Symp. Proc.* 375, 201–206 (1995).
- P. M. Mooney, F. K. LeGoues, and J. L. Jordan-Sweet, "Dislocation Nucleation Barrier in SiGe/Si Structures Graded to Pure Ge," *Appl. Phys. Lett.* 65, No. 22, 2845–2847 (1994).
- J. L. Jordan-Sweet, P. M. Mooney, M. A. Lutz, R. M. Feenstra, J. O. Chu, and F. K. LeGoues, "Unique X-Ray Diffraction Pattern at Grazing Incidence from Misfit Dislocations in SiGe Thin Films," *J. Appl. Phys.* 80, No. 1, 89–96 (1996).
- 26. P. M. Mooney, J. A. Ott, J. O. Chu, and J. L. Jordan-Sweet, "X-Ray Diffraction Analysis of SiGe/Si Heterostructures on Sapphire Substrates," *Appl. Phys. Lett.* 73, 924–926 (1998); P. M. Mooney, J. O. Chu, J. A. Ott, J. L. Jordan-Sweet, W. B. Dubbelday, K. L. Kavanagh, I. Lagnado, and B. S. Meyerson, "Analysis of SiGe FET Device Structures on Silicon-on-Sapphire Substrates by X-Ray Diffraction," *Mater. Res. Soc. Symp. Proc.* 533, 55–59 (1998).
- P. M. Mooney, J. L. Jordan-Sweet, K. Ismail, J. O. Chu, R. M. Feenstra, and F. K. LeGoues, "Relaxed Si_{0.7}Ge_{0.3} Buffer Layers for High-Mobility Devices," *Appl. Phys. Lett.* 67, No. 16, 2373–2375 (1995).
- P. H. Fuoss and S. Brennan, "Surface Sensitive X-Ray Scattering," Ann. Rev. Mater. Sci. 20, 365–390 (1990).
- G. B. Stephenson, K. F. Ludwig, Jr., J. L. Jordan-Sweet, S. Brauer, J. Mainville, Y. S. Yang, and M. Sutton, "Instrumentation for Millisecond-Resolution Scattering Studies," *Rev. Sci. Instrum.* 60, 1537–1540 (1989).
- L. A. Clevenger, R. A. Roy, C. Cabral, Jr., K. L. Saenger, S. Brauer, G. Morales, K. F. Ludwig, Jr., G. Gifford, J. Bucchignano, J. Jordan-Sweet, P. DeHaven, and G. B. Stephenson, "A Comparison of C54–TiSi₂ Formation in Blanket and Submicron CMOS Gate Structures Using *In Situ* X-Ray Diffraction During Rapid Thermal Annealing," *J. Mater. Res.* 10, 2355–2359 (1995).

- C. Lavoie, C. Caral, Jr., L. A. Clevenger, J. M. E. Harper, J. Jordan-Sweet, K. L. Saenger, and F. Doany, "Light Scattering Measurement of Surface Topography During Formation of Titanium Silicide," *Mater. Res. Soc. Symp. Proc.* 406, 163–168 (1996).
- L. A. Clevenger and R. W. Mann, "Titanium Silicides and Their Technological Applications," *Mater. Res. Soc. Symp. Proc.* 320, 15–25 (1994).
- 33. R. W. Mann, L. A. Clevenger, P. D. Agnello, and F. R. White, "Silicides and Local Interconnections for High-Performance VLSI Applications," *IBM J. Res. Develop.* 39, 403–417 (1995).
- 34. J. B. Lasky, J. S. Nakos, O. J. Cain, and P. J. Geiss, "Comparison of Transformation to Low Resistivity Phase and Agglomeration of TiSi₂ and CoSi₂," *IEEE Trans. Electron Devices* **38**, 262–269 (1991).
- G. L. Miles, R. W. Mann, and J. E. Bertsch, "TiSi₂ Phase Transformation Characteristics on Narrow Devices," *Thin Solid Films* 290–291, 469–472 (1996).
- R. W. Mann and L. A. Clevenger, "The C49 to C54 Phase Transformation in TiSi₂ Thin Films," *J. Electrochem. Soc.* 141, 1347–1350 (1994).
- Z. Ma, L. A. Allen, and D. D. J. Allman, "Microstructural Aspects and Mechanism of the C49-to-C54 Polymorphic Transformation in Titanium Disilicide," *J. Appl. Phys.* 77, 4384–4388 (1995).
- R. W. Mann, G. L. Miles, T. A. Knotts, D. W. Rakowski, L. A. Clevenger, J. M. E. Harper, F. M. d'Heurle, and C. Cabral, Jr., "Reduction of the C54-TiSi₂ Phase Transformation Temperature Using Refractory Metal Ion Implantation," *Appl. Phys. Lett.* 67, 3729-3731 (1995).
- C. Cabral, Jr., L. A. Clevenger, J. M. E. Harper, F. M. d'Heurle, R. A. Roy, and K. L. Saenger, "Lowering the Formation Temperature of the C54-TiSi, Phase Using a Metallic Interfacial Layer," J. Mater. Res. 12, No. 2, 304-307 (1997); C. Cabral, Jr., L. A. Clevenger, J. M. E. Harper, R. A. Roy, K. L. Saenger, G. L. Miles, and R. W. Mann, "In Situ X-Ray Diffraction Analysis of TiSi, Phase Transformation from a Titanium-Molybdenum Bilayer," Mater. Res. Soc. Symp. Proc. 441, 295-300 (1997).
- C. Cabral, Jr., L. A. Clevenger, J. M. E. Harper, F. M. d'Heurle, R. A. Roy, C. Lavoie, K. L. Saenger, G. L. Miles, R. W. Mann, and J. S. Nakos, "Low Temperature Formation of C54–TiSi2 Using Titanium Alloys," *Appl. Phys. Lett.* 71, 3531–3533 (1997).
- A. Mouroux, S.-L. Zhang, W. Kaplan, S. Nygren, M. Ostling, and C. S. Petersson, "Enhanced Formation of the C54 Phase of TiSi₂ by an Interposed Layer of Molybdenum," *Appl. Phys. Lett.* 69, 975–977 (1996).
- 42. C. Cabral, Jr., L. A. Clevenger, R. A. Roy, G. B. Stephenson, C. Lavoie, K. L. Saenger, J. Jordan-Sweet, R. Viswanathan, G. Morales, and K. L. Ludwig, Jr., "In-Situ X-Ray Diffraction Analysis of CoSi₂ Phase Formation on Single and Polycrystalline Silicon as a Function of Linewidth and Dopant at Rapid Thermal Annealing Rates," Advanced Metallurgy and Interconnect Systems for ULSI Applications, 1995 ULSI XI Conference Proceedings, Materials Research Society, 1996, pp. 439–445; C. Cabral, Jr., L. A. Clevenger, G. B. Stephenson, S. Brauer, G. Morales, and K. F. Ludwig, Jr., "In-Situ X-Ray Diffraction and Resistivity Analysis of CoSi₂ Phase Formation with and without a Ti Interlayer at Rapid Thermal Annealing Rates," Mater. Res. Soc. Symp. Proc. 375, 253–258 (1995).
- I. C. Noyan, J. L. Jordan-Sweet, E. G. Liniger, and S. K. Kaldor, "Microbeam Diffraction Studies of Interfacial Strain," *National Synchrotron Light Source Activity Report* 1997, Brookhaven National Laboratory publication BNL-52540, E. Z. Rothman and J. B. Hastings, Eds., New York, 1998, pp. 2–7.

- I. C. Noyan, J. Jordan-Sweet, E. G. Liniger, and S. K. Kaldor, "Characterization of Substrate/Thin-Film Interfaces with X-Ray Microdiffraction," *Appl. Phys. Lett.* 72, 3338–3340 (1998).
- J. L. Jordan-Sweet, İ. C. Noyan, E. Liniger, S. K. Kaldor, and P.-C. Wang, "Characterization of Strain in Thin-Film Structures with Microdiffraction," Adv. X-Ray Anal. 42 (in press).
- P.-C. Wang, I. C. Noyan, S. K. Kaldor, J. L. Jordan-Sweet, E. G. Liniger, and C.-K. Hu, "Measurement of Electromigration-Induced Stress Gradient in Aluminum Conductor Lines," *Appl. Phys. Lett.* (in press).
- 47. P. M. Mooney, J. L. Jordan-Sweet, I. C. Noyan, S. K. Kaldor, and P.-C. Wang, "Observation of Local Tilted Regions in Strain-Relaxed SiGe/Si Buffer Layers Using X-Ray Microdiffraction," *Appl. Phys. Lett.* 74, 726 (1999); P. M. Mooney, J. L. Jordan-Sweet, I. C. Noyan, S. K. Kaldor, and P.-C. Wang, "Images of Local Tilted Regions in Strain-Relaxed Si Ge Layers," *Phys. B* 273-274, 608 (1999).
- I. C. Noyan, P.-C. Wang, S. K. Kaldor, and J. L. Jordan-Sweet, "Deformation Field in Single-Crystal Semiconductor Substrates Caused by Metallization Features," *Appl. Phys. Lett.* 74, 2352 (1999).
- I. C. Noyan, S. K. Kaldor, J. Jordan-Sweet, and P.-C. Wang, "A Cost-Effective Method for Minimizing the Sphere-of-Confusion Error of X-Ray Microdiffractometers," Rev. Sci. Instrum. 70, 1300 (1999).
- I. C. Noyan, P.-C. Wang, S. K. Kaldor, J. L. Jordan-Sweet, and E. G. Liniger, "Divergence Effects in Monochromatic X-Ray Diffraction Using Tapered Capillary Optics," Rev. Sci. Instrum. (in press).
- B. D. Cullity, Elements of X-Ray Diffraction, 2nd ed., Addison-Wesley Publishing Co., Reading, MA, 1978, pp. 140, 268–269.

Received April 14, 1999; accepted for publication September 21, 1999 Jean L. Jordan-Sweet IBM Research Division, Thomas J. Watson Research Center, P.O. Box 218, Yorktown Heights, New York 10598 (jljs@us.ibm.com). Dr. Jordan-Sweet is a Research Staff Member in the Silicon Technology Department at the Thomas J. Watson Research Center. She received a B.S. degree in physics and chemistry from Loyola University at Los Angeles in 1976, and a Ph.D. in physical chemistry from the University of California at Los Angeles in 1983. The following year she joined IBM in the Packaging Department of the Thomas J. Watson Research Center. Her work involved the use of photoemission techniques to study metal-polymer interfaces at the National Synchrotron Light Source (NSLS) of Brookhaven National Laboratory. Dr. Jordan-Sweet subsequently became the Resident Scientist and Manager of the IBM/MIT X-ray research facility at Port X20 of the NSLS. Her current interests include the application of a wide range of X-ray diffraction techniques to study thin films and interfaces of materials used in microelectronic device fabrication.